The Usefulness of MSU3 Analyses as a Forecasting Aid: A Statistical Study

PAUL A. HIRSCHBERG,* MATTHEW C. PARKE, CARLYLE H. WASH, AND MARK MICKELINC

Department of Meteorology, Naval Postgraduate School, Monterey, California

ROY W. SPENCER

Earth System Science Division, NASA/Marshall Space Flight Division, Huntsville, Alabama

ERIC THALER

National Weather Service, Denver, Colorado

(Manuscript received 13 September 1996, in final form 18 February 1997)

ABSTRACT

A statistical analysis is performed on a 6-month global dataset consisting of satellite-derived channel 3 Microwave Sounding Unit (MSU3) brightness temperature and various conventionally derived fields to quantify the potential usefulness of MSU3 analyses in the nowcasting and forecasting of baroclinic waves. High positive spatial and temporal correlations are obtained between the MSU3 brightness temperature and 400–100-mb thickness fields over all wavelengths in the data. Slightly lesser positive correlations are found between the MSU3 and the 200-mb temperature. The MSU3–500-mb and MSU3–50-mb height correlation results indicate a scale dependence in the hydrostatic spreading of thickness anomalies in the vertical. Most significantly, relatively high negative MSU3–500-mb height correlations for the short ($\leq$ synoptic scale) wavelength portion of the data suggest that upper-level thermal anomalies are reflected downward and that MSU3 analyses can be used to track midlevel synoptic-scale baroclinic waves. This conclusion is also supported by relatively high negative MSU3–500-mb vorticity and MSU3–dynamic tropopause correlations along the climatological storm tracks.

1. Introduction

The forecasting of extratropical cyclones and the associated weather patterns is still a challenging problem for operational meteorologists. This is especially true for locations over eastern ocean basins and western continents where the accuracy of analyses and numerical guidance is limited by regions of conventional data sparsity upstream. On a routine basis, space-based remote sensors are the only feasible method to acquire information that can improve the forecast problem over these regions. Qualitative satellite information, such as visible, infrared, and water vapor imagery, has already proven its value in this regard. More significantly, there is also a large reservoir of quantitative information that can be obtained from satellite measurements.

Traditionally, quantitative satellite information has been available in the form of high horizontal, but low vertical resolution, Television Infrared Observation Satellite (TIROS) Operational Vertical Sounder (TOVS) temperature soundings. These soundings are retrieved from satellite radiance data and a knowledge of the vertical weighting function characteristics of the spectral frequencies measured by the onboard sensor in question. Unfortunately, observing system sensitivity experiments with modern data assimilation systems suggest that these ''retrieved'' satellite soundings do not produce great improvement in forecast skill and in some cases actually result in decreased skill (e.g., Flobert et al. 1991). One reason for these disappointing results, besides the inherent limitations of data quality and low vertical resolution, is the errors that are introduced by the ill-posed inversion process from observed radiance values to temperature profiles (e.g., Eyre and Lorenc 1989). Furthermore, tropospheric temperature soundings cannot be confidently retrieved in areas of precipitation that are common in the vicinity of cyclones.

In light of the current problems with converting satellite measurements into pseudoradiosonde soundings, techniques are now being sought to more directly utilize the information that satellite sensors provide. For ex-

* Current affiliation: National Weather Service, Silver Spring, Maryland.

Corresponding author address: Paul A. Hirschberg, National Weather Service, 1325 East–West Highway, Building SSMC2, Room 13236, Silver Spring, MD 20910.
E-mail: Paul.Hirschberg@noaa.gov

ample, Velden (1992) and Spencer et al. (1995) show that satellite microwave radiance observations can be used to depict important features and processes in the upper troposphere and lower stratosphere. This region of the atmosphere is a significant reservoir of potential vorticity (PV). The structure of the upper-level PV field, specifically the structure of anomalous PV near the tropopause, plays a critical role in the dynamics of tropospheric weather systems (e.g., Hoskins et al. 1985). Whereas previous studies (e.g., Shapiro et al. 1982; Uccellini et al. 1985) have utilized once per day satellite ozone measurements from the Total Ozone Mapper Spectrometer (TOMS) instrument to locate positive PV anomalies associated with tropopause folds, Velden (1992) demonstrates the applicability of utilizing 54.96-GHz channel (channel 3) Microwave Sounding Unit (MSU) brightness temperature (T_b) imagery to infer the position, size, orientation, and relative strength of tropopause-level thermal anomalies. These warm and cold anomalies that lie over the low and under the high portions of tropopause undulations, respectively, are dynamically linked to PV anomalies and are also directly related to the hydrostatic structure and development of baroclinic waves and cyclones (Hirschberg and Fritsch 1991a,b). Synoptic-scale tropospheric troughs and low pressure centers are hydrostatically induced underneath stratospheric warm (low density) pools (see also Bell and Bosart 1993) and are deepened by strong tropopause-level warm (negative density) advection (e.g., Hirschberg and Fritsch 1991a,b, 1993a,b, 1994; Jusem and Atlas 1991; Luppo et al. 1992; Martin et al. 1993; Hirschberg and Doyle 1995).

Both the Velden (1992) and Spencer et al. (1995) studies suggest that the channel 3 MSU (MSU3) observations that are available every 6 h may be a valuable diagnostic tool that can be used to monitor the progression of upper-level features in numerical simulations of cyclone events over conventional data-sparse regions, especially when used in conjunction with other satellite-derived products (see also Claud et al. 1995). However, their conclusions are based on subjective comparisons between the MSU3 T_b and conventional fields during only a few selected extratropical cyclone events. To firmly establish the credibility of this new analysis product, more objective comparisons must be performed during many events. In this paper, we begin this quantification by statistically correlating horizontal analyses and time series of MSU3 T_b fields to horizontal and time series of various conventionally derived fields over the Northern Hemisphere middle latitudes (25°–65°N) during the 6-month period 1 October 1993–31 March 1994.

2. Data processing

The MSU is flown aboard the *TIROS-N* series of National Oceanic and Atmospheric Administration (NOAA) polar-orbiting satellites. The unit consists of a four-channel passive microwave system that measures

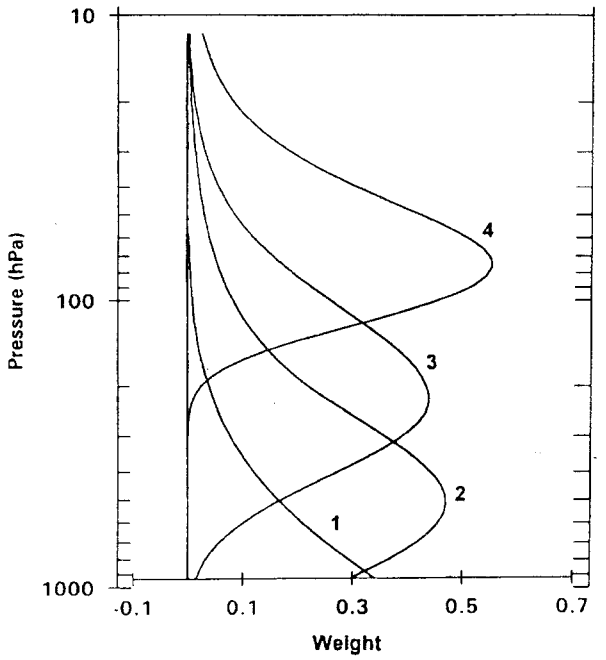

FIG. 1. Vertical profile of weighting functions for MSU channels 1–4. The weight equals the change of transmittance with $\log_e(p)$. From Spencer et al. (1995).

the thermal emission in the oxygen absorption region (Rao et al. 1990). The radiance measurements from channel 3 of the MSU represent a layer average (400–100-mb) T_b owing to the weighting function characteristics of the channel (Fig. 1). Significantly, minimal attenuation of the channel 3 signal from cloud and ice precipitation enables successful utilization of the information obtained from this channel even in extensively cloudy and precipitating conditions when other sensors such as the High Resolution Infrared Sounder may fail (Velden 1992).

Ground stations can receive local MSU data in real time as the polar orbiters pass overhead. In addition, global MSU data from all passes are collected and distributed by the National Environmental Satellite Data Information Service in near-real time to various centers including the Marshall Space Flight Center (MSFC). *NOAA-11* and *-12* satellite midlatitude passes between 25° and 65°N and within 3-h windows centered at 0000 and 1200 UTC were extracted from the MSFC archive and processed for the 6-month period 1 October 1993–31 March 1994. This 6-month period was chosen because of the relatively high baroclinic activity expected during the fall and winter months of the Northern Hemisphere.

The MSU provides 11 individual measurements (footprints) across its cross-track swath width of approximately 2200 km (Spencer et al. 1995). The footprints are spaced about 150 km apart in both the along-track and cross-track directions. At nadir, each footprint has a spatial resolution of about 110 km. As the MSU scans

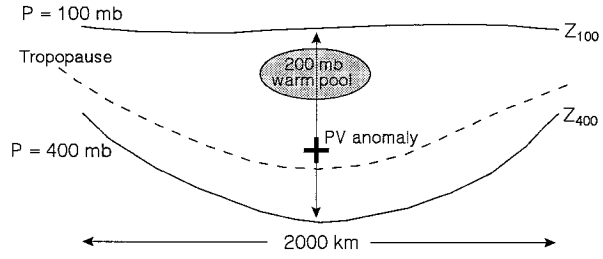

FIG. 2. Schematic pressure vs horizontal distance diagram illustrating atmospheric features associated with a positive temperature anomaly in the 400–100-mb layer. Here, Z_{100} and Z_{400} are the 100- and 400-mb geopotential heights, respectively. The 200-mb warm pool associated with the low portion of a tropopause undulation is stippled, and the positive potential vorticity anomaly is indicated with a plus sign.

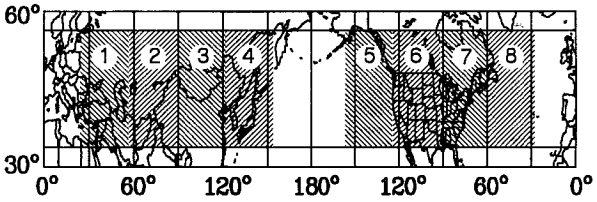

FIG. 3. The climatology domain used in the calculation of spatial correlation coefficients between the MSU3 T_b and various conventionally derived fields at each map time. Stippled regions with number indicate the eight areas over which spatial correlation coefficients were calculated.

away from nadir, the footprints become more elliptical and larger, reaching about 200 km across at the edges of the swath. To remove small scan-to-scan biases, the MSU3 T_b data were calibrated according to a procedure similar to the one outlined in Spencer et al. (1990), except that an average of three scan lines of calibration information instead of only one was used to calibrate each scan line of data (Spencer et al. 1995). The cold bias or ''limb darkening'' that occurs in the off-nadir measurements was corrected following the technique described by Spencer et al. (1995). Rather than correcting the nonnadir measurements to nadir as is the traditional approach, the corrections were performed relative to the intermediate earth incidence angle of 33° [footprint positions 3 and 9 in Fig. 2 of Spencer et al. (1995)]. This intermediate correction procedure performs better than a nadir correction because it involves a smaller range of deviations from the view angle to which it is applied (for more details see Spencer et al. 1995). A consistent approximately 2-K bias that was found between the *NOAA-11* and *NOAA-12* MSU3 data (*NOAA-12* warmer than *NOAA-11*) was corrected by applying latitudinally smoothed offsets to the *NOAA-12* MSU3 T_bs. These offsets were calculated by first averaging the MSU3 T_bs for both satellites over 10° wide global–latitude bands for each of the 6 months in the study period. Offsets were determined by subtracting the resulting averaged *NOAA-11* T_bs from the *NOAA-12* T_bs.

A multiquadric interpolation scheme (Nuss and Titley 1994) was used to objectively analyze the processed MSU3 T_b data on a regular 2.5° latitude by 2.5° longitude (145 × 17) grid centered at 45°N, 180° at every 0000 and 1200 UTC map time. The multiquadric technique uses radial hyperboloid functions to fit scattered data to the regular grid and has been found by Nuss and Titley (1994) to be more accurate than either the Cressman (1959) or the Barnes (1973) objective analysis schemes in tests of analytic functions.

Corresponding 12-h conventional analyses of the fields listed in Table 1 were obtained from the National Centers for Environmental Prediction (NCEP, formerly known as the National Meteorological Center) Global Data Assimilation System (GDAS) on the same grid at mandatory levels. Derived fields of vorticity, PV, dynamic tropopause (pressure value of the 1.5×10^{-6} m^2 s^{-1} K kg^{-1} PV surface) and 400–100-mb thickness were also calculated. These particular fields were chosen for several reasons. As a consequence of its weighting function characteristics, the MSU3 T_b anomaly signatures should be highly correlated with upper-level thickness and temperature anomalies. As Velden (1992) qualitatively demonstrates, horizontal analyses of the T_b data can locate and track tropopause-level thermal anomalies. However, the hydrostatic analysis of Hirschberg and Fritsch (1991a,b, 1993a) suggests that the spatial locations and relative intensities of lower-stratospheric warm pools should also reflect the positions and relative

TABLE 1. Conventional fields obtained and derived from the NCEP GDAS.

Sea level pressure (mb)
1000–500 mb thickness (mb)
400–100 mb thickness (m)
250-mb temperature (°C)
200-mb temperature (°C)
500-mb height (m)
400-mb height (m)
100-mb height (m)
50-mb height (m)
500-mb vorticity (s^{-1})
100-mb vorticity (s^{-1})
300-mb isentropic pot. vorticity (m^2 s^{-1} K kg^{-1})
Dynamic tropopause (1.5×10^{-6} m^2 s^{-1} K kg^{-1})

TABLE 2. The number of valid map times utilized in the calculation of spatial correlation coefficients between the channel 3 MSU and selected conventional fields.

Area	No. valid map times
1	211
2	352
3	343
4	199
5	211
6	354
7	342
8	206

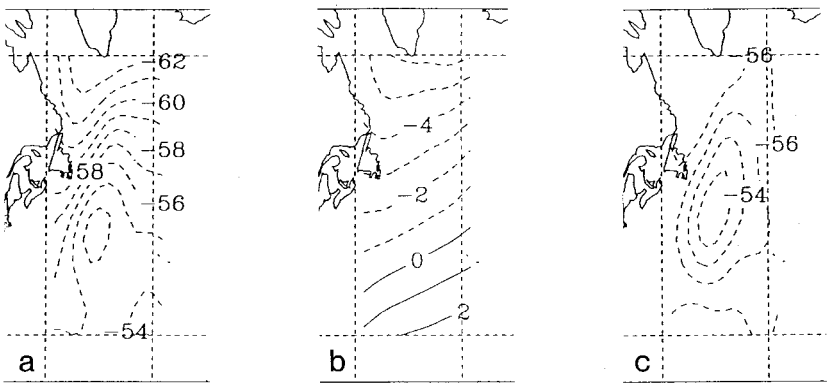

FIG. 4. An example of (a) total (AL), (b) trend-only (TR), and (c) trend-removed (DTR) MSU3 T_b analyses (°C) for area 8.

strengths of synoptic-scale upper-level geopotential, vorticity, and potential vorticity features (Fig. 2). Obviously, high correlations between the MSU3 T_b analyses and these conventional fields would provide important additional nowcasting and forecasting information, especially at off-synoptic times and over data-sparse regions. The ability of the MSU3 data to locate and track tropopause-level PV anomalies would be of particular value.

3. Statistics

Two sets of 6-month correlations were compiled. The first were spatial correlations between MSU3 T_b and the conventional (Table 1) field analyses for every 12-h map time. The second were temporal correlations between 12-h MSU3 T_b and conventional field time series at individual gridpoint locations. Although there should be redundancies in the spatial and temporal statistics, each

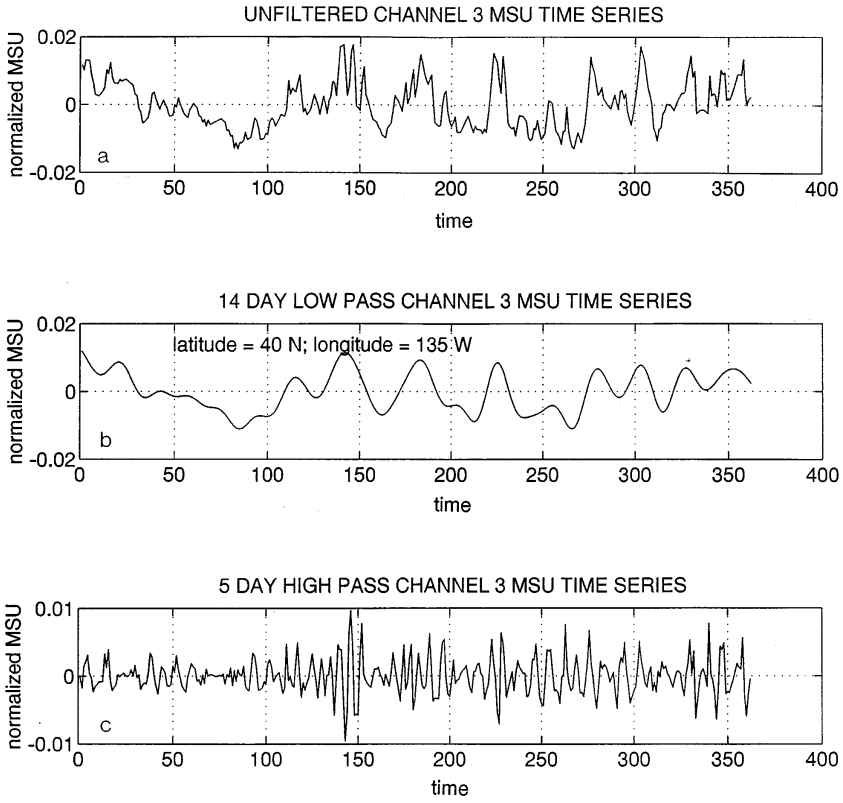

FIG. 5. An example of an (a) unfiltered (UF), (b) 14-day low-pass (LP) filtered and (c) 5-day high-pass (HP) filtered MSU3 T_b time series at one grid point. Time is in 12-h increments beginning 0000 UTC 1 October 1993 through 1200 UTC 31 March 1994.

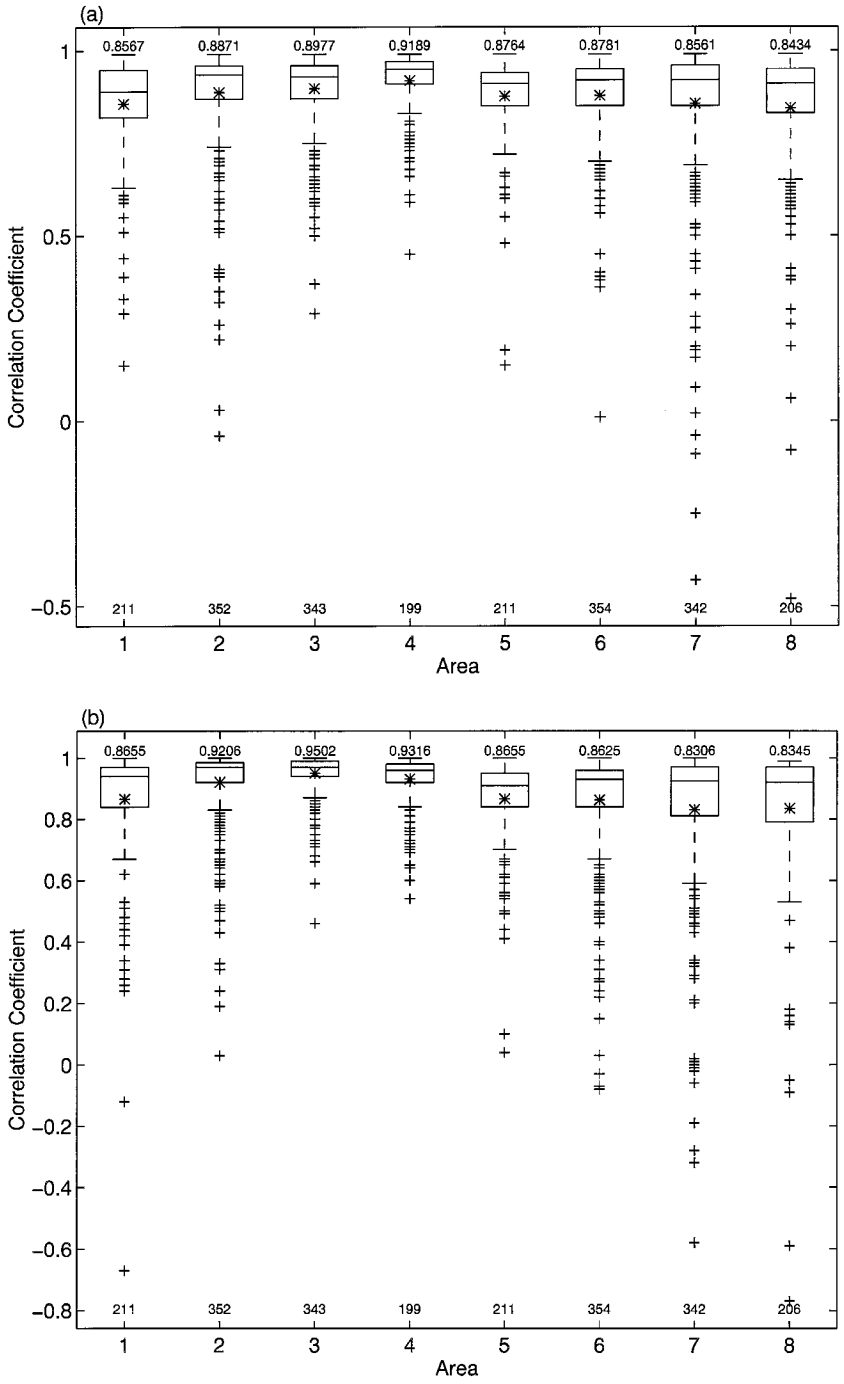

FIG. 6. Box plots of area-average correlation coefficients between all valid time (AVT) MSU3 T_b and 400–100-mb thickness AL (a), TR (b), and DTR (c) area (see Fig. 3) analyses during the 6-month period 1 October 1993–31 March 1994. The ordinate is the correlation coefficient. The abscissa numbers correspond to areas 1–8. Box plots indicate grouping of data values. The lower boundary of each box marks the 25th percentile and the upper boundary marks the 75th percentile. The upper dashed line extends to the upper adjacent value that is less than or equal to the 75th percentile plus 1.5 times the range of the middle 50% of the data. The lower dashed line extends to the lower adjacent value that is greater than or equal to the 25th percentile plus 1.5 times the range of the middle 50% of the data. The median, mean, and extreme values for each area sample are denoted by a horizontal line, an asterisk, and plus signs, respectively. Means are also listed on the top of each box plot and data sample numbers for each area are listed at the bottom.

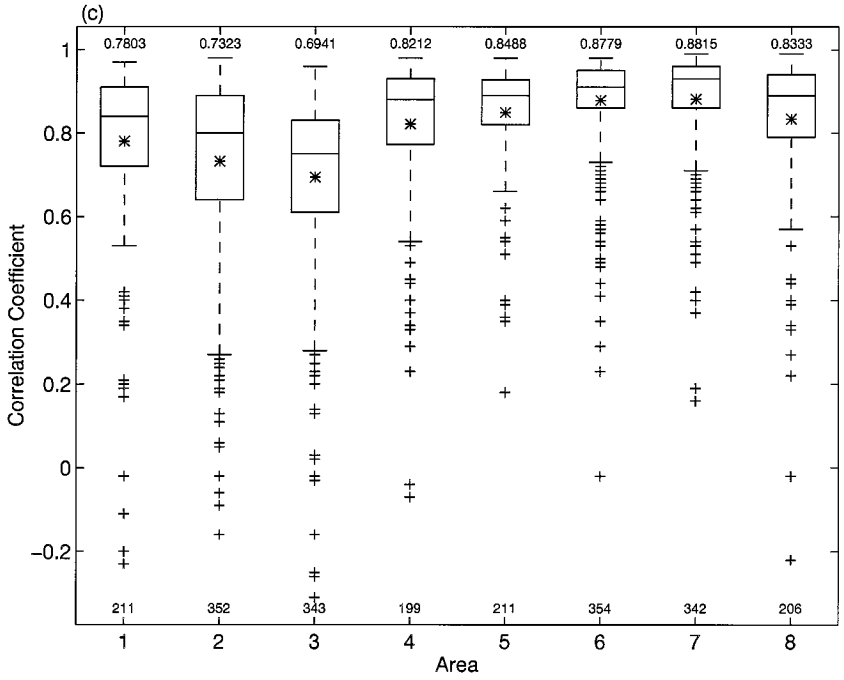

FIG. 6. (*Continued*)

set of results provides insights that the other set does not. For example, the spatial correlation coefficients show how well the MSU3 and conventional analyses compare at individual map times, but over relatively large geographic areas; whereas the horizontal analyses of the temporal correlation coefficients illuminate more detailed information concerning the geographic distribution of correlations, but over a large time period.

a. Spatial correlations

The spatial correlation coefficients between the MSU3 T_b and the conventional field analyses were calculated for eight $30° \times 30°$ (13×13 grid points) subdomains or areas (Fig. 3). The areas were chosen to compare data-sparse regions with data-rich regions. This subdivision also allowed for a gross evaluation of the effects of surface type (land vs water) as well as terrain effects on the correlations.

There were a possible 364 (0000 and 1200 UTC) map times during the 6 months. However, not all of these times (depending on area) were available for processing owing to the criterion that the *NOAA-11* or *NOAA-12* satellite pass time over an area had to be within 3-h windows centered at 0000 or 1200 UTC. In addition, a criterion that at least 75% of the area of interest had to be covered by satellite observations at each valid time was applied, which further reduced the number of available map times. Consequently, a total of between 199 and 354 ''valid'' times were analyzed over the 6-month period depending on the area (Table 2). In particular, over 50% of the possible map times were used in the calculation of the spatial correlation coefficients for areas over western Asia and the western Pacific and North Atlantic Oceans. Better than 90% coverage was obtained over central Asia and North America. Additionally, owing to the specific orbital paths, most of the MSU3 data were obtained from the 1200 UTC map time window for areas 1 and 8. Conversely, the Pacific region (areas 4 and 5) primarily used MSU3 data within the 0000 UTC window. Other areas (central Asia, North America) had an even mix of both 0000 and 1200 UTC MSU3 data over the 6 months. Fortunately, as will be discussed in section 4, comparison of the results for those areas with predominately 0000 and 1200 UTC data (e.g., areas 5 and 8, respectively) indicates that the map time distribution did not have an effect on the average spatial correlation coefficients that were calculated.

It was also of interest to investigate scale dependencies present in the data. The size (2400 km $\times$ 3300 km) of the eight areas provided a natural filter for synoptic-scale features upon removal of latitudinal and longitudinal trends in the data. In particular, each area analysis was decomposed into two portions, a large-scale or trend (TR) portion and a small-scale or detrended (DTR) portion. The detrended portion was determined following the method of Errico (1985). This method removes the large, unresolved scales from any field f and results in a field that contains only wavelengths less than or equal to the domain size, and is periodic in both the i and j directions. The linear trends are defined by the boundary values of the original field and are removed by first determining the zonal slope of the field for each row j with

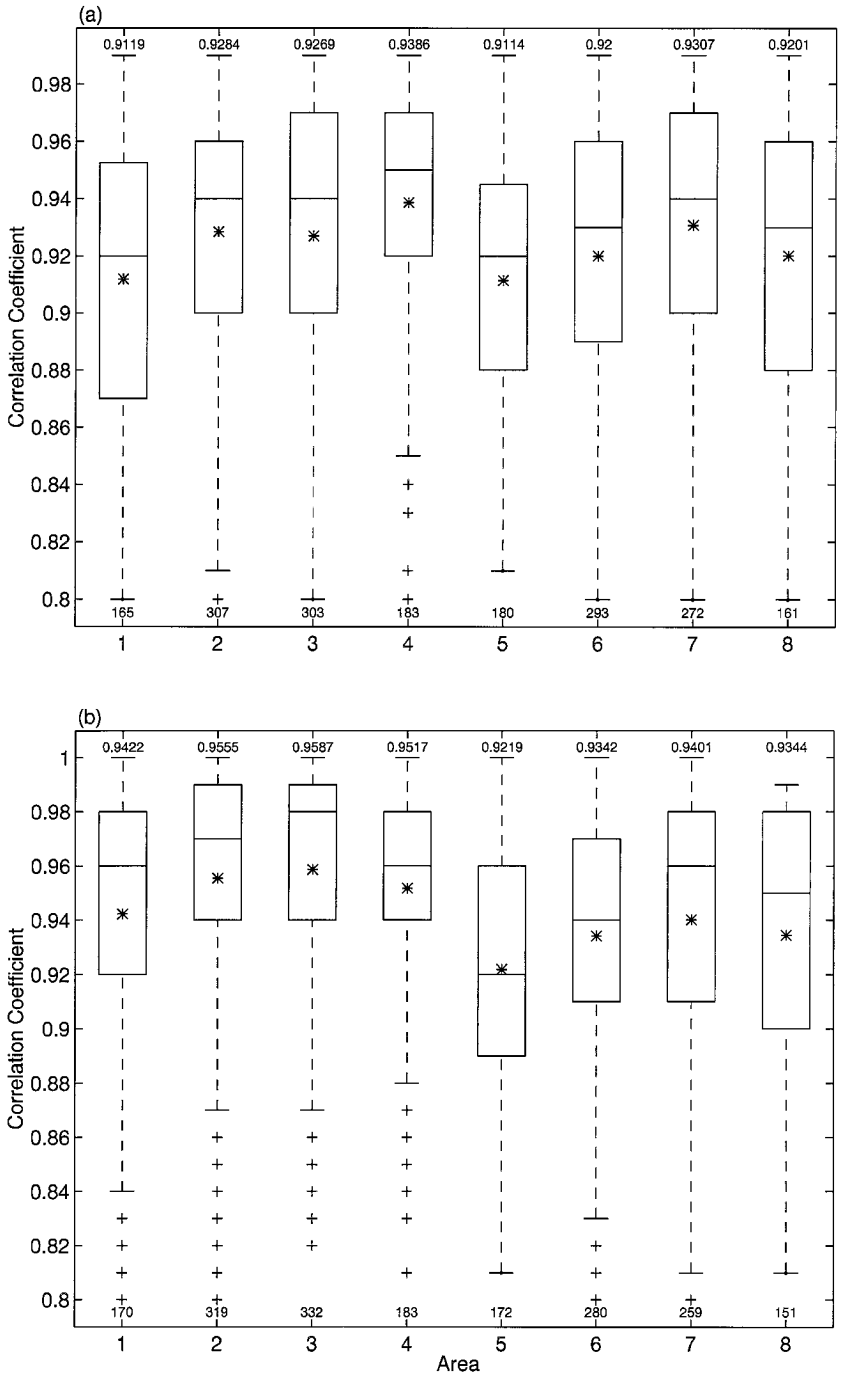

FIG. 7. As in Fig. 6 except for only those map times when the thickness correlation coefficient (TC) is ≥0.80.

$$s_j = \frac{f_{N_I,j} - f_{1,j}}{N_I - 1}, \tag{1}$$

where s_j is the slope and N_I the width of row j. In the present case $N_I = 13$ for all j. The trends in the i direction are removed from the original field at every i, j by applying

$$f'_{i,j} = f_{i,j} - 0.5(2i - N_I + 1)s_j, \tag{2}$$

where $f'_{i,j}$ is the zonally detrended value of $f_{i,j}$. Last, the roles of i and j are reversed to detrend the field in the meridional direction with the $f'_{i,j}$ from (2) replacing the $f_{i,j}$ in (1). This procedure results in a field detrended in both directions. The TR or large-scale portion of the

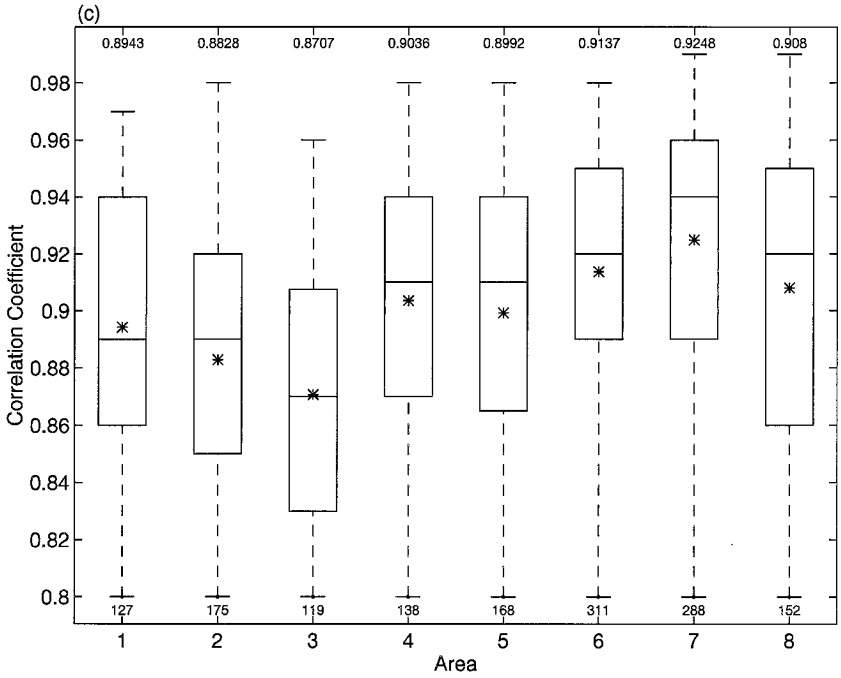

FIG. 7. (*Continued*)

analysis is recovered by subtracting the small-scale DTR analysis from the original total field (AL) analysis. An example of an AL, TR, and DTR MSU3 T_b analysis is shown in Fig. 4.

Correlation coefficients (Dixon and Massey 1969) were computed for the AL, TR, and DTR analyses with

$$\rho_a^c = \rho_a(m, c) = \frac{\mathrm{Cov}_a(m, c)}{\sqrt{S_a^2(m)S_a^2(c)}}, \tag{3}$$

where ρ_a^c is the correlation coefficient for area a between the MSU3 T_b analysis m and the conventional analysis c of interest, Cov_a is the area covariance, and S_a^2 is the area variance. Prior to calculation of the correlation coefficient with (3), the MSU3 T_b and conventional field data were normalized by removal of the subdomain mean from the fields. Finally, 6-month-average correlation coefficients $\overline{\rho}_a^c$ were determined for each area by summing the available 12-h coefficients over the 6 months and dividing by the number of analysis times.

b. Temporal correlations

Temporal correlation coefficients between the MSU3 T_b and the conventional field time series were calculated at all gridpoint locations containing at least 115 days (330 12-h values) of satellite data. To investigate scale dependencies in the time series, high- and low-pass elliptical filters were first applied to the data at each grid point. Wave periods were selected that produced synoptic-scale filtered series and longer than synoptic-scale filtered series. In particular, the low-pass filter was designed to pass waves with periods longer than 14 days, while a separate high-pass filter was designed to pass waves with periods shorter than 5 days.

According to Yates and Bateman (1989), the elliptic filter provides excellent attenuation compared to other filters (e.g., Butterworth, Chebyshev) for a given filter order. However, a drawback of the elliptic filter is its poor phase response (Yates and Bateman 1989). Obviously, phase errors introduced by the filtering process would contaminate the correlations. Fortunately, there are techniques that can be applied to the filtering process that reduce the phase errors induced by the use of finite time series with a finite transit start-up time. The problem was alleviated in the 6-month dataset by first padding the start and end times of the MSU3 T_b and conventional field series with zeros after normalizing these data by removing the time series means. Then, the series was ''normally'' filtered (i.e., forward in time), followed by a second pass where the output of the forward filtering step was reversed in time and again passed through the filter. The above steps produced a filtered series where all frequencies had zero phase shifts. An example of an unfiltered (UF), low- (LF), and high-pass filtered (HP) MSU3 time series is presented in Fig. 5.

Temporal correlation coefficients were calculated for the UF, LP, and HP time series at each grid point i, j, with

$$\rho_{i,j}^c = \rho_{i,j}(m, c) = \frac{\mathrm{Cov}_{i,j}(m, c)}{\sqrt{S_{i,j}^2(m)S_{i,j}^2(c)}}, \tag{4}$$

where $\rho_{i,j}^c$ is the temporal correlation coefficient for grid point i, j between the MSU3 T_b time series m and con-

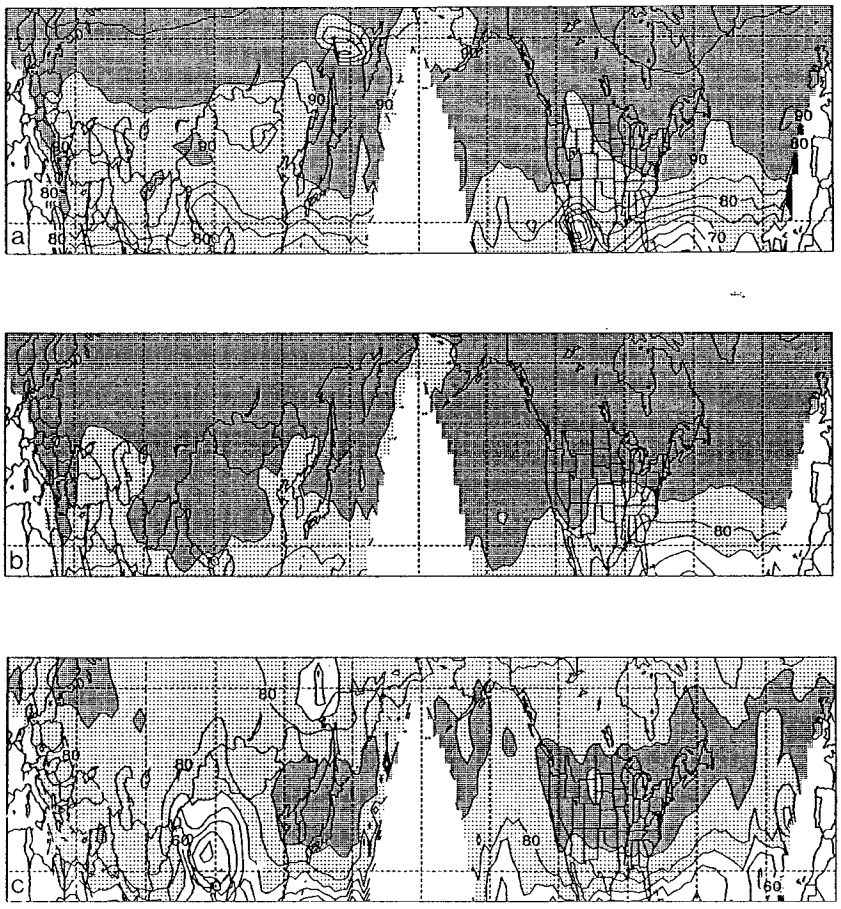

FIG. 8. Analysis of (a) UF, (b) 14-day LP filtered, and (c) 5-day HP filtered 6-month temporal correlation coefficients (solid, contour interval 10^{-2}) between the MSU3 T_b and 400–100-mb thickness.

ventional time series c; $\mathrm{Cov}_{i,j}$ is the temporal covariance; and $S^2_{i,j}$ is the temporal variance. In both the spatial and temporal calculations, a Student's t-test (Dixon and Massey 1969) was used to verify that the correlations were statistically significant at the 99% level.

4. Results

In this section, the 6-month spatial and temporal correlation coefficients between the MSU3 T_b and various conventional fields are presented. At the outset, one concern might be that correlations between the MSU and conventional analyses will be misleading since TOVS soundings, which include MSU information, are incorporated into the NCEP fields particularly in analyses over the oceans. However, the TOVS soundings are dominated by the larger number of spectral channels associated with the infrared (IR) system while the microwave information is weighted in a more limited manner (C. S. Velden 1996, personal communication). Furthermore, these IR-dominated soundings are not utilized in areas of inclement weather where the MSU3 data often remain uncontaminated (Velden 1992). Finally, the NCEP GDAS incorporates a significant number of aircraft observations (Kanamitsu 1989) in the analyses of upper-tropospheric and lower-stratospheric levels.

Since there were redundant results in the correlations when comparing the MSU3 T_bs to similar conventional fields (e.g., the 500-mb geopotential height and 400-mb geopotential height fields), we limit the presentation and discussion of the results to only those comparisons found to be most enlightening: the MSU3 T_bs and the 1) 400–100-mb thickness, 2) 200-mb temperature, 3) 500-mb geopotential height, 4) 50-mb height, 5) 500-mb vorticity, 6) dynamic tropopause, and 7) sea level pressure fields. While additionally, in the interest of brevity, the statistics of selected comparisons are conveyed in the form of box plots all of the 6-month average spatial correlation coefficients for each of the eight areas (Fig. 3) are presented in tabular form in the appendix. In particular, 6-month average area correlations are listed in the tables for the AL, TR, and DTR analyses for each area. The corresponding temporal correlation between the 6-month MSU3 UF, LP, and HP T_b and conventional

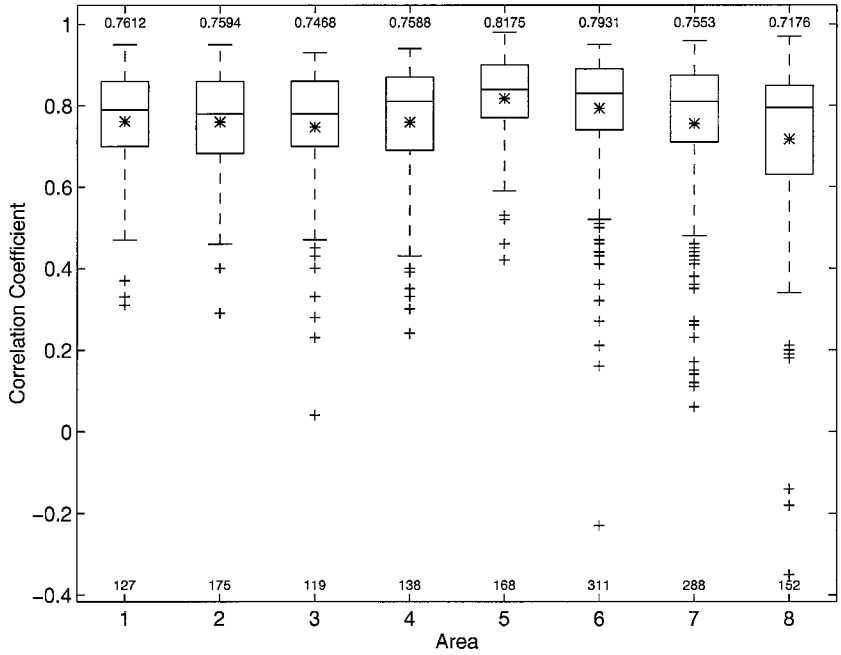

FIG. 9. As in Fig. 6 except for DTR MSU3 T_b and 200-mb temperature correlation coefficients and for only those map times when TC $\geq$ 0.80.

field time series are presented in the form of horizontal analyses.

a. MSU3 T_b and 400–100-mb thickness

Since the MSU3 radiances represent a layer-averaged T_b between 400 and 100 mb, it is not surprising to find generally high positive average spatial correlations between the MSU3 T_b analyses and the 400–100-mb thickness analyses for all areas and horizontal scales (Fig. 6 and Table A1). In particular, the AL analysis average correlations with all valid times (AVT) considered (Fig. 6a) range between 0.84 (area 8, northwestern Atlantic) and 0.92 (area 4, east Asia and adjacent waters). For the large-scale TR analyses (Fig. 6b), the correlations range between 0.83 (area 8, northwestern Atlantic) and 0.95 (area 3, central Asia). Less positive correlation coefficients are found in the small-scale DTR analyses (Fig. 6c), particularly over the Eastern Hemisphere.

Motivated by the existance of clearly outlying low MSU3 and 400–100-mb thickness correlation values in the data (Fig. 6), the area-average correlation coefficients were also separated into two groups for each area. The first group consisted of the average coefficients of those map times that had a thickness correlation coefficient TC $\geq$ 0.80. The second group average consisted of the remaining map times with TC $<$ 0.80. This segregation of map times was done in an attempt to identify suspect analysis times. That is, the supposition was made that there was a data or analysis problem if the MSU3 T_b–400–100-mb thickness correlation was unduly low (TC $<$ 0.80) and that further comparison between the MSU3 T_b and the other conventional fields (e.g., 500-mb height) at these times should not be considered. Not surprisingly, the average spatial correlations increased substantially over all horizontal scales and areas for the TC $\geq$ 0.80 grouping (Fig. 7 and Table A1). Approximately 83% of the AL map times fell into this category (Table A1). Curiously, the area 2 and 3 DTR results show relatively high percentages of 50% and 65%, respectively, of suspect analysis times. This result is not entirely clear although some hypotheses will be presented later that concern the apparent discrepancies in the correlation results over the eastern Eurasian continent.

The MSU3 T_b and 400–100-mb thickness field temporal correlations over the 6-month period show generally high positive coefficients over the entire global domain and for all wavelengths (Fig. 8). This result is consistent with the high positive 6-month average spatial correlation findings. Specifically, the UF analysis (Fig. 8a) exhibits no correlation $<$0.70, while half the domain shows coefficients of 0.90 or better. The LP analysis (Fig. 8b) suggests even stronger positive correlation between the long-wavelength portion of the MSU3 T_b–400–100-mb thickness signal. Similarly, the HP analysis (Fig. 8c) shows generally high positive temporal correlation between the MSU3 T_b and the 400–100-mb thickness fields. This particular analysis is interesting for a number of reasons. Whereas the UF (Fig. 8a) and LP (Fig. 8b) analyses exhibit increases in the

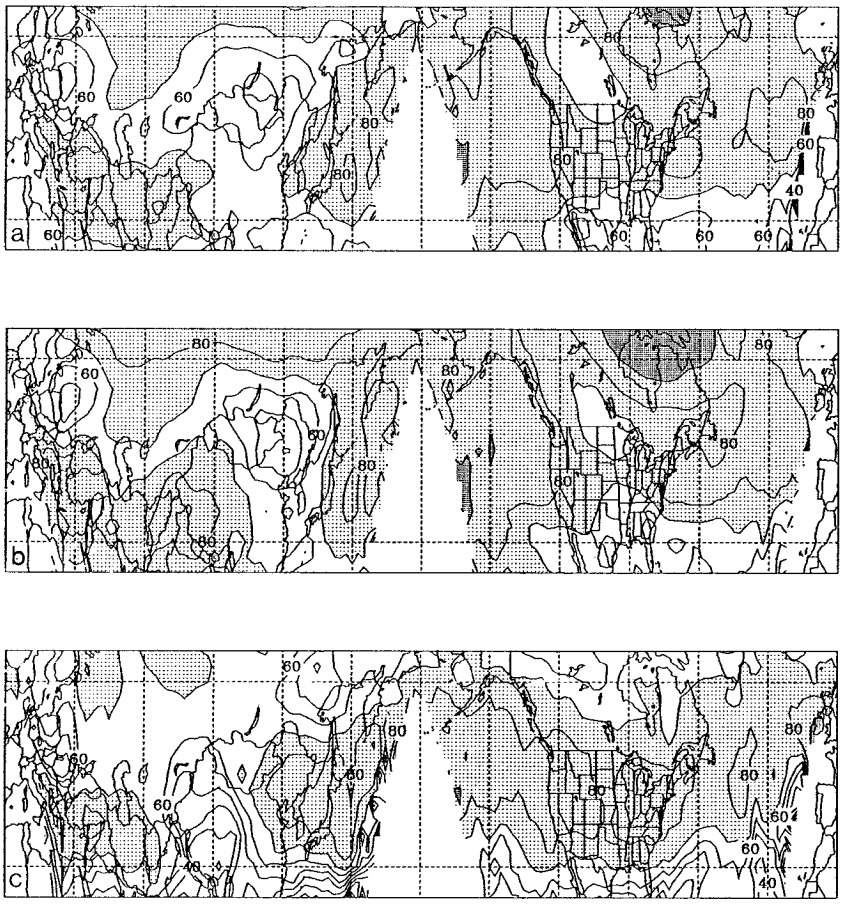

FIG. 10. As in Fig. 8 except for MSU3 T_b and 200-mb temperature correlation coefficients.

positive correlations toward higher latitudes, the HP analysis (Fig. 8c) shows a general decrease of correlation toward higher latitudes. Strikingly, at the shorter timescales captured by the HP analysis, the sense of the climatological ''storm tracks'' is evident as correlation bands of higher than 0.90 generally tend northeastward from east Asia to the Aleutians and from the western United States to the northwestern Atlantic. There is also a clear center of lower correlations across the Tibetan plateau near 90°E. This indicates that the MSU3 T_b data are either contaminated by high-topography surface emission or that the NCEP GDAS analyses are poorer in this area. Since the MSU senses microwave energy at midlevels of the atmosphere, it can potentially be contaminated over regions that contain topography (e.g., the Himalayas) that reach these levels.

One of the goals of this study was to ascertain whether a conventional data-rich-region versus data-poor-region (e.g., land–sea) contrast would exist in the correlations between the MSU3 T_b and conventional fields. It was speculated that the correlations would drop over conventional data-poor regions, particularly upstream of radiosonde networks. There is some hint of this in the HP MSU3 T_b–400–100-mb thickness correlation results (Fig. 8c) over the northeastern Pacific. However, it appears that the correlations are more dependent on the climatological storm track than any influence that poorer oceanic analyses may have. Perhaps this suggests that the analyses over data-sparse regions are influenced more by upper-level aircraft observations and the MSU3 satellite data than previously thought.

b. MSU3 T_b and 200-mb temperature

The relatively high correlations between the MSU3 T_b and 400–100-mb thickness fields suggest that the MSU should be also highly correlated with isobaric temperature patterns within the layer. Hirschberg and Fritsch (1991a,b) find the strongest temperature anomalies associated with tropopause undulations to be typically near 200 mb. The 6-month data confirm that although the MSU3 T_b–200-mb temperature spatial correlations are less positive than the layer-average temperature correlations reflected by the 400–100-mb thickness, they are the largest of any individual level in the 400–100-mb layer (other levels not shown). Spe-

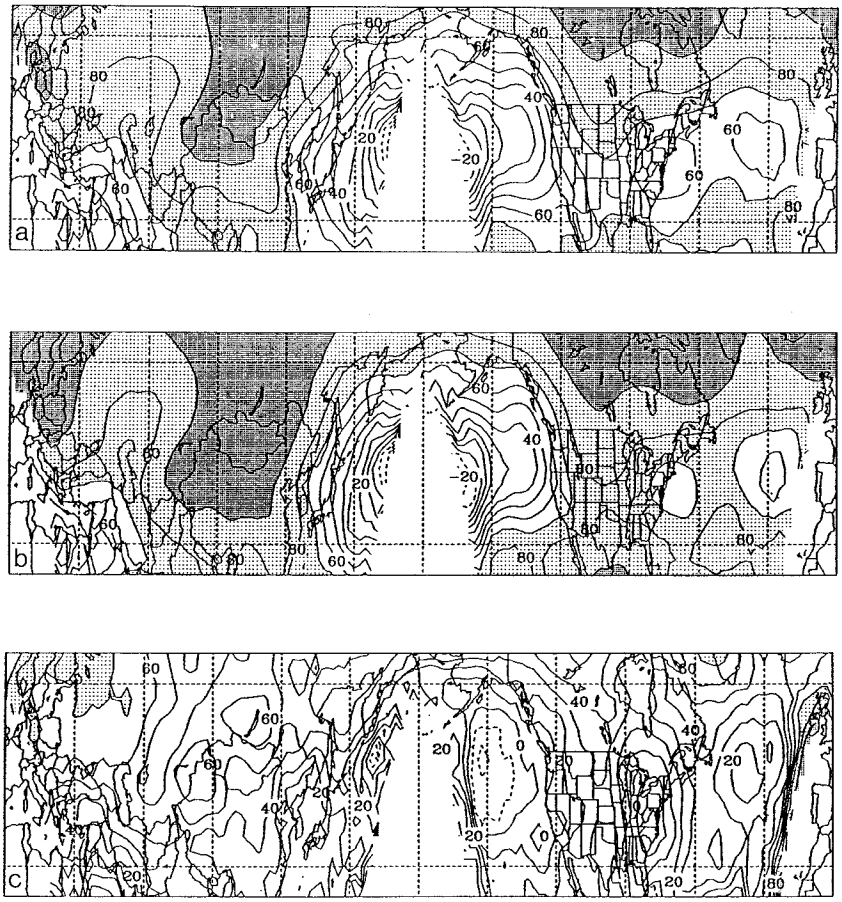

FIG. 11. As in Fig. 8 except for MSU3 T_b and 50-mb height correlation coefficients.

cifically, the largest 200-mb temperature spatial correlations (average over all areas = 0.77) are found in the DTR fields when the TC $\geq$ 0.80 criterion is applied (Fig. 9 and Table A2). Overall, the geographic distribution of 200-mb correlations is similar to the thickness correlations (Fig. 7 and Table A1) with highest correlations occurring over western North America (area 5) and the lowest over central Asia (Area 3).

Consistent with the spatial results, the temporal correlation analyses of MSU3 T_b and 200-mb temperature (Fig. 10) also indicate relatively high positive correlation over much of the global domain. When the data are high-pass filtered to remove the wavelengths with periods >5 days (Fig. 10c), high positive correlations (>0.80) are found over eastern Asia and the Western Hemisphere. Significantly, these high positive correlations suggest that the MSU3 T_b fields can be used to track synoptic-scale tropopause-level thermal anomalies with a high degree of confidence.

c. MSU and 500- and 50-mb heights

The potential utility of the MSU3 T_b data in diagnostic and forecasting applications is perhaps better illuminated by examining the correspondence between the MSU3 T_b and geopotential height patterns at individual isobaric levels. The relationship between isobaric-layer temperature anomalies and geopotential height anomalies that bracket the layer depends on how the associated average temperature (thickness) anomaly manifests hydrostatically in the vertical geopotential height distribution. For instance, a warm anomaly between 400 and 100 mb would be associated with a positive geopotential height anomaly at 100 mb (higher heights) if the 400-mb geopotential field was held fixed and relatively uniform (no anomalies). In a sense, the accompanying positive thickness anomaly would be ''spread'' upward in the geopotential height field. Conversely, such a positive thickness (warm temperature) anomaly would be spread downward and result in a negative geopotential height anomaly at 400 mb (lower heights) if the 100-mb geopotential field was fixed and relatively uniform.

Hirschberg and Fritsch (1993b) suggest that the vertical direction and magnitude of thickness spreading is scale dependent. They demonstrate with an analytic model that the spreading occurs primarily downward

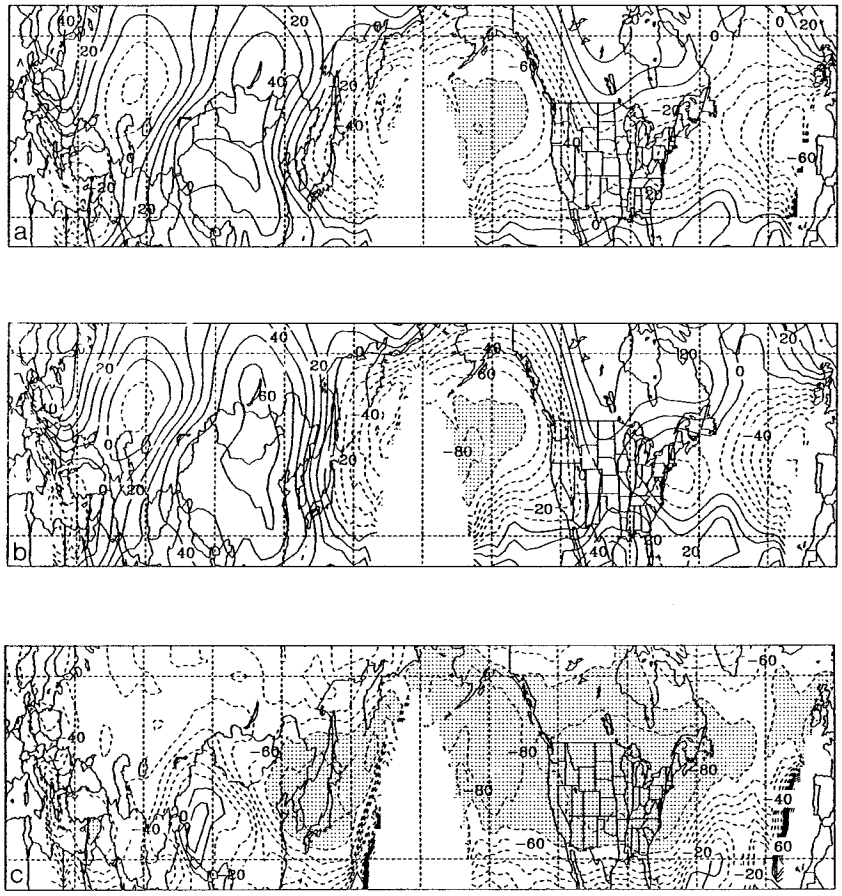

FIG. 12. As in Fig. 8 except for MSU3 T_b and 500-mb height correlation coefficients.

for flows with synoptic-scale wavelengths less than approximately 5000 km and increasingly upward for larger scale flows. They use this scale-dependence argument to hypothesize the existence of a stratospheric level of insignificant dynamics (LID) where the geopotential height tendencies at synoptic time and space scales are insignificant (Hirschberg and Fritsch 1991a,b, 1993a,b, 1994). Given the existence of a LID, they explain how upper-level temperature anomalies associated with synoptic-scale undulations in the tropopause can hydrostatically induce height anomalies below them.

To examine whether vertical thickness spreading is evident in the MSU data, we first consider the MSU3 T_b and 50-mb height and MSU3 T_b and 500-mb height temporal correlations in Figs. 11 and 12, respectively. Specifically, the UF (Fig. 11a) and, to an even greater extent, the LP (Fig. 11b) analyses show relatively high positive correlations between the MSU3 T_bs and the 50-mb heights over most of the domain. Conversely, relatively little correlation is evident between the MSU3 T_bs and the 500-mb heights in the UF (Fig. 12a) and LP (Fig. 12b) analyses aside from an area over the central and eastern North Pacific where relatively high negative correlations (<-0.70) are found. Therefore, the temporal analyses are generally consistent with the idea that large-scale thermal anomalies are spread upward. That is, long-wavelength thermal anomalies tend to affect the geopotential heights above them.

Conversely, the synoptic-scale wavelength ($\leq$5-day period) temporal signals in the 6-month MSU3 T_bs and the height fields suggest that short-wavelength thermal anomalies are spread downward and tend to affect geopotential heights below them. Specifically, the MSU3 T_b–50-mb height correlations (Fig. 11c) decrease across the whole domain, while high negative correlations (≤-0.70) between the MSU3 T_bs and the 500-mb heights (Fig. 12c) become dominant aside from the notable exception over the Tibetan plateau. A region of negative correlations (≤-0.80) from eastern Asia to the northwestern Atlantic again outline the sense of the favored synoptic-scale storm tracks. In terms of the potential application to forecasting, the temporal correlations results suggest that small-scale ($\leq$synoptic scale) warm (cold) anomalies in the MSU3 T_bs correspond well

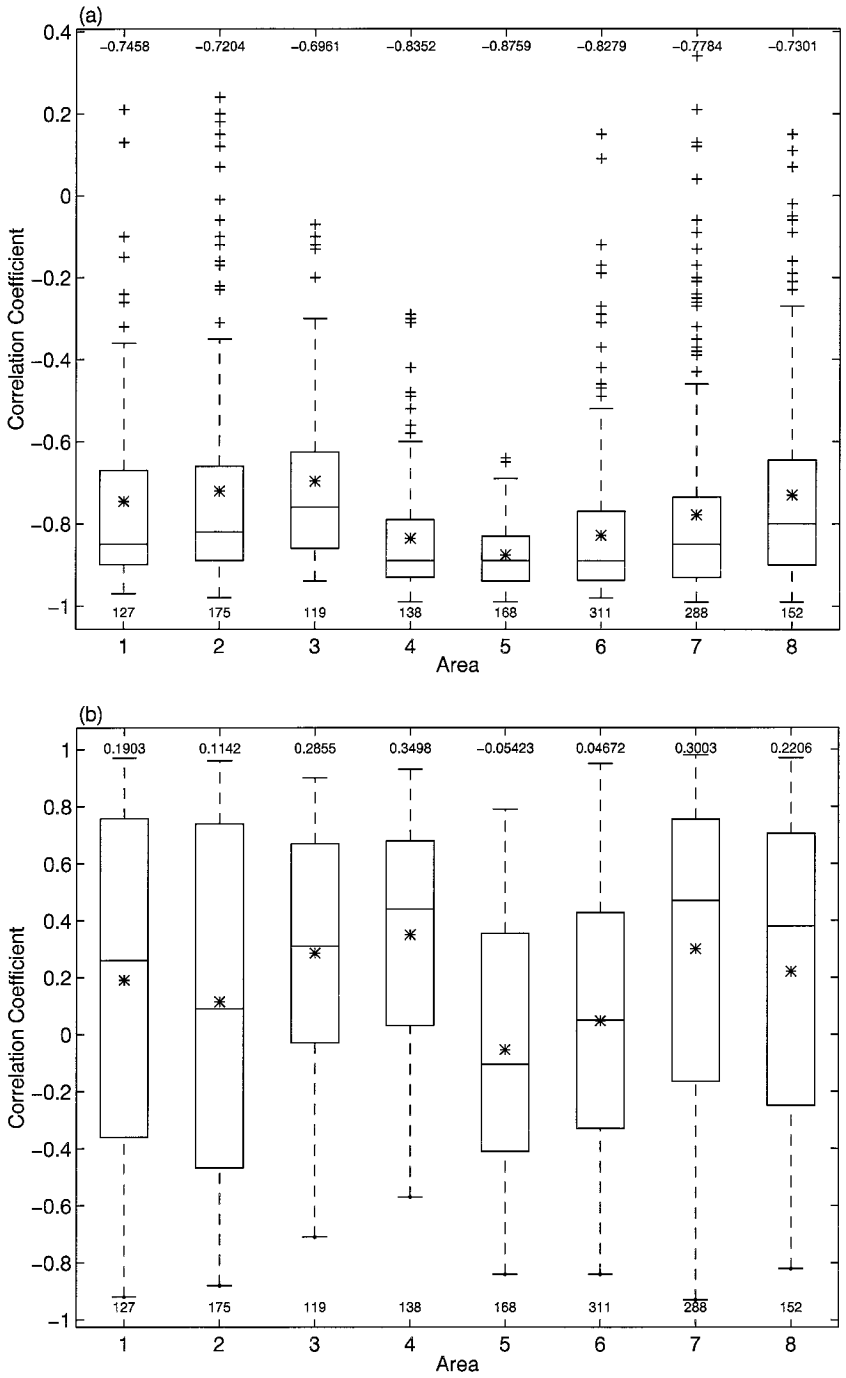

FIG. 13. As in Fig. 6 except for (a) DTR MSU3 T_b and 500-mb height correlation coefficients, and (b) DTR MSU3 T_b and 50-mb height correlation coefficients, and for only those times when TC $\geq$ 0.80.

with small-scale trough (ridge) features in the 500-mb height pattern.

The scale dependency between tropopause-level temperature anomalies and the direction of the thickness spreading should also be evident in the spatial correlations. That is, the DTR (smaller scale) MSU3 T_b patterns should be more highly negatively correlated with the 500-mb geopotential height patterns and the TR (larger scale) MSU3 T_b patterns should be more highly positively correlated with the 50-mb geopotential height patterns. Although the spatial correlations are certainly suggestive of these expected results, they are less so

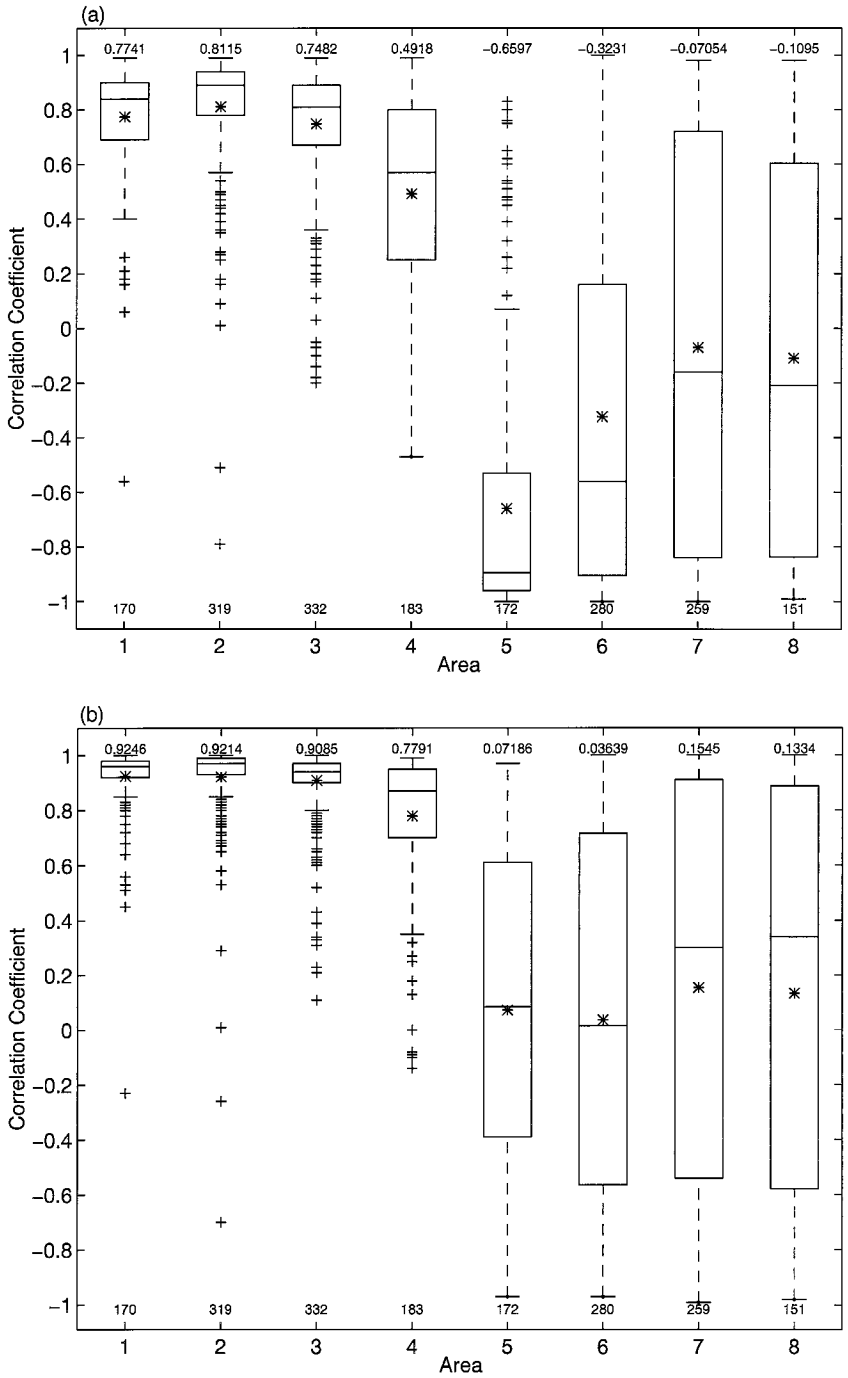

FIG. 14. As in Fig. 6 except for (a) TR MSU3 T_b and 500-mb height correlation coefficients and (b) TR MSU3 T_b and 50-mb height correlation coefficients and for only those times when TC $\geq$ 0.80.

when compared to the temporal results. In particular, the DTR MSU3 T_b and 500-mb height analyses do show consistent negative correlations across all areas (Table A3). In the Eastern Hemisphere (EH) with AVT considered, the average correlation is -0.61 while in the Western Hemisphere (WH) the average increases to -0.74. Significantly the application of the TC $\geq$ 0.80 criterion exposes even higher negative correlations between the DTR MSU3 T_bs and 500-mb heights (Fig. 13a and Table A3). The average correlations increase to -0.75 over the EH and -0.81 over the WH when the suspect map times are excluded. Also, consistent

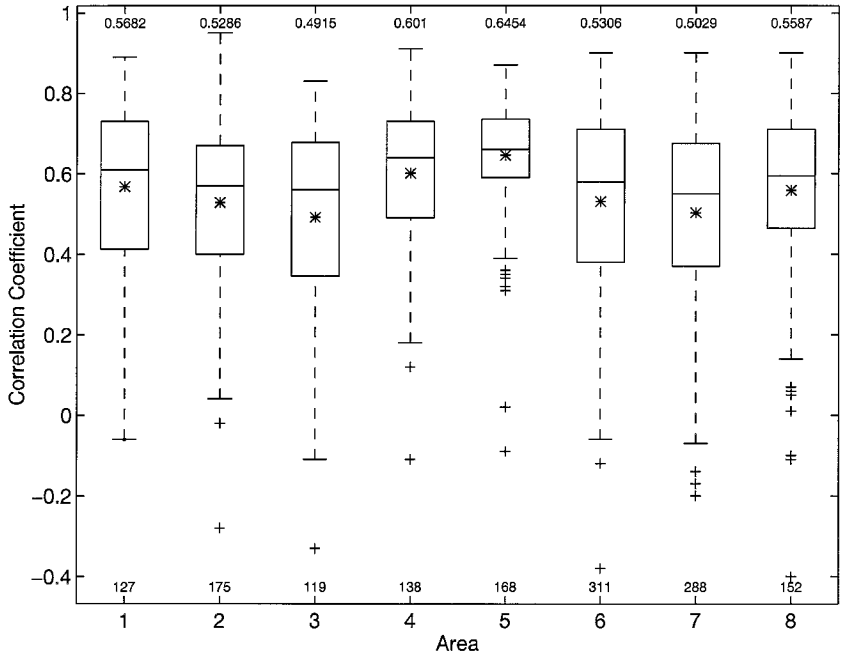

FIG. 15. As in Fig. 6 except for DTR MSU3 T_b and dynamic tropopause correlation coefficients and for only those times when TC $\geq$ 0.80.

with the scale argument are the DTR MSU3 T_bs and 50-mb height correlations (Fig. 13b, and Table A4) for the EH and WH, which indicate small correlation (average = 0.18) between the DTR MSU3 T_bs and 50-mb height fields when the TC $\geq$ 0.80 criterion is applied.

However, the correlation coefficients pertaining to TR (large scale) fields (Fig. 14a and Table A4) show relatively high positive coefficients between the MSU3 T_bs and the 500-mb geopotential heights over the EH (average = 0.71 when the TC $\geq$ 0.80 criterion is applied). This result is difficult to interpret based on the scale-dependence argument although it might be linked to deep thermal anomalies in lower layers of the atmosphere. Conversely, in the WH, the TR results seem to agree with the scale-dependence argument although there is a large spread in the data. Specifically, the TR 500-mb geopotential height analyses are less correlated with the TR MSU3 T_bs (average = -0.29 when the TC $\geq$ 0.80 criterion is applied).

Finally, we should also expect to find the TR MSU3 T_b patterns to be more highly correlated in a positive sense with the 50-mb geopotential height patterns than the DTR patterns. As expected, the TR analyses exhibit high positive correlations (Fig. 14b, Table A4) over the EH, with an average of 0.88 when the TC $\geq$ 0.80 criterion is applied. However, the TR analyses fields indicate no correlation (average = 0.10) over the WH (Fig. 14b and Table A4) although there is much spread in the data. This discrepancy between the EH and WH results is curious and merits further consideration.

d. MSU and 500-mb vorticity and dynamic tropopause

The 500-mb vorticity field has traditionally been an important analysis product in the forecasting of baroclinic waves and surface cyclones (e.g., Petterssen 1956). The MSU3 T_b–500-mb height correlations presented in the previous section suggest that the MSU3 thermal patterns should also be related to the synoptic-scale 500-mb vorticity field. A new analysis product, which is perhaps more dynamically revealing than midlevel vorticity (Hoskins et al. 1985), is an analysis of the isobaric level of the dynamic tropopause (e.g., Hoskins and Berrisford 1988). Specifically, positive (negative) PV anomalies along isentropic surfaces near the tropopause correspond to low-cold (high-warm) dynamic tropopauses and midlevel positive (negative) relative vorticity centers. Hirschberg and Fritsch (1991b) show that relatively low (high) tropopauses are consistent with the presence of warm (cold) anomalies in the upper troposphere and lower stratosphere. Therefore, the MSU3 T_b pattern should show correspondence to the tropopause pattern as well.

The 6-month-average correlations between the MSU3 and 500-mb vorticity and the MSU3 and the dynamic tropopause analyses are presented in the appendix (Tables A5 and A6, respectively). Both sets of correlations are consistent since the 500-mb vorticity pattern is in reality an out-of-focus reflection of the tropopause-level PV distribution (Hoskins et al. 1985). All subdomains

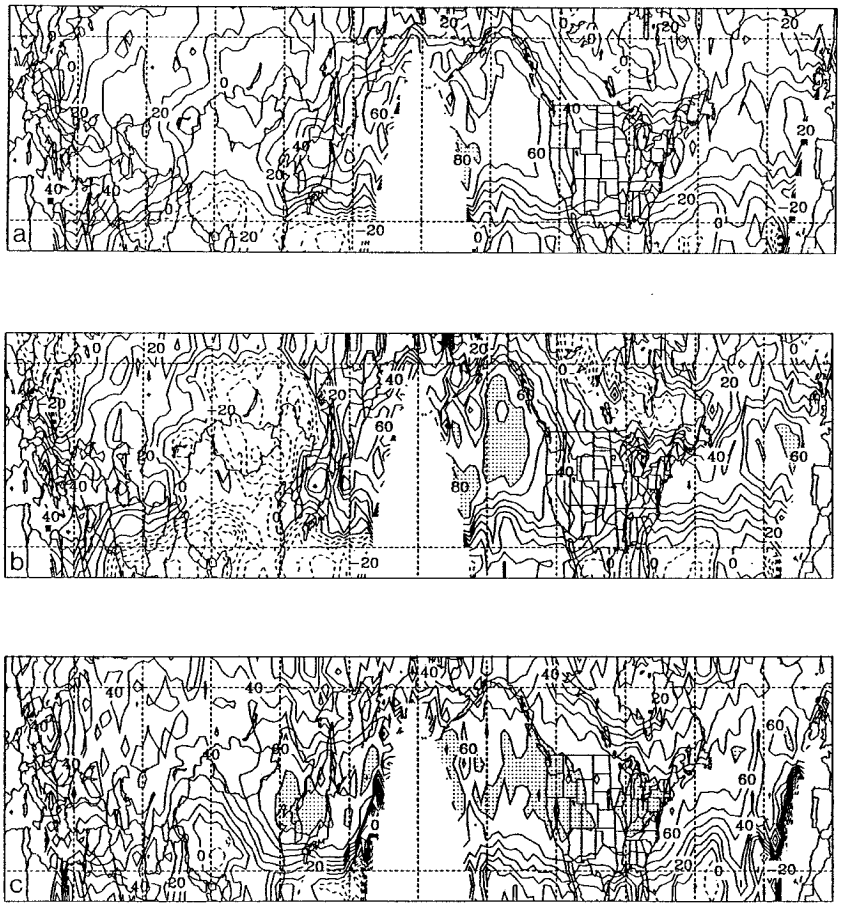

FIG. 16. As in Fig. 8 except for MSU3 T_b and dynamic tropopause correlation coefficients.

show weak correlations between the MSU and vorticity and tropopause analyses except for the eastern Pacific (area 5). Here the AVT and TC ≥ 0.80 correlations are >0.65. Interestingly, the EH and WH AL correlations tend to be opposite signed. However, as with the 500-mb height correlations, there appears to be a scale dependency in the relationship between the MSU and the 500-mb vorticity and tropopause patterns. While the large-scale TR correlations tend to reflect those for the AL, the small-scale DTR correlations exhibit a definite positive sense especially for cases when the TC ≥ 0.80 is applied (e.g., Fig. 15). However, the eastern Pacific (area 5) exhibits no significant difference between AL, DTR, and TR analyses (Tables A5 and A6). Unfortunately, it is beyond the scope of this study to attempt a detailed explanation for this particular result. However, a possible reason might be the synoptic regime that dominated this portion of the world during the 6-month period. In particular, occluded synoptic-scale disturbances present in the DTR fields may tend to be more coupled with the large-scale disturbances present in both the AL and the TR fields.

Similar to the spatial results, the MSU3 T_b 500-mb vorticity and MSU3 T_b–dynamic tropopause temporal correlations are consistent with one another and with the height field comparisons. The UF and LF analyses show generally low positive correlations between the MSU3 T_b and the dynamic tropopause (Figs. 16a,b), although an area of relatively high positive correlation appears again over the central and northwestern Pacific Ocean. Consistent with the scale-dependence hypothesis, a pattern of higher positive correlations emerges, especially in the MSU3 T_b–dynamic tropopause analysis (Fig. 16c), after the data have been put through the 5-day high-pass filter to exclude longer than synoptic-scale disturbances. In particular, >0.70 correlations are evident across the storm tracks from eastern Asia to the northwestern Atlantic.

e. MSU and sea level pressure

Finally, we examine the spatial relationship between the MSU3 T_b and sea level pressure analyses. Over the life cycle of a typical surface cyclone, the spatial relationship between features associated with the upper-level dynamics (i.e., upper-level PV anomalies, strato-

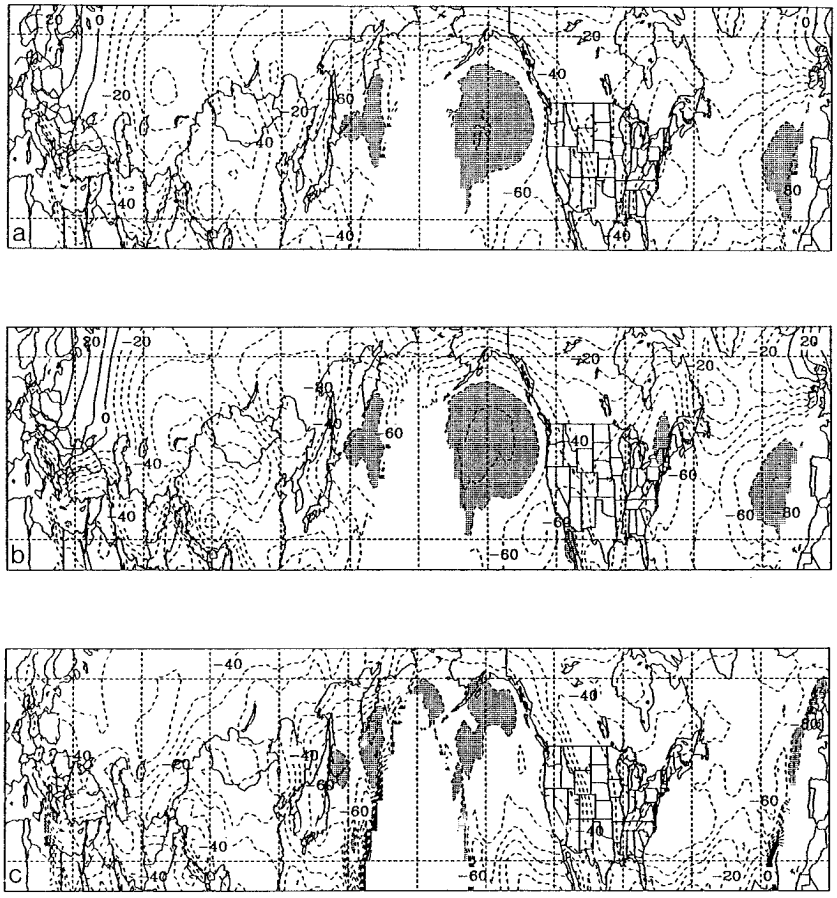

FIG. 17. As in Fig. 8 except for MSU3 T_b and sea level pressure correlation coefficients.

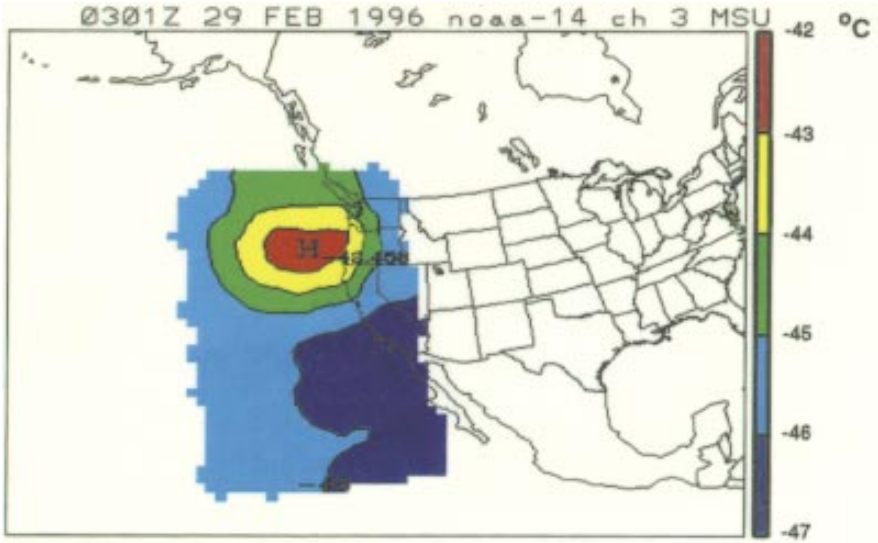

FIG. 18. An example of the West Coast MSU3 T_b analysis (°C) displayed in real time at the Naval Postgraduate School web site. The relatively warm (red) T_bs off the Oregon coast in this analysis correspond to a tropopause-level positive PV anomaly and are associated with a midlevel vortex and geopotential trough.

spheric warm pools, 500-mb vorticity centers, etc.) and the surface low varies. In particular, Hirschberg and Fritschs (1991b) conceptual model (see their Fig. 25) 959describes how the relationship between tropopause-level thermal anomalies and surface lows change during baroclinic development. During the initial stages of cyclogenesis, warm pools associated with the low portions of tropopause undulations are often found upstream of the nascent surface low. As development proceeds, this phase lag decreases until occlusion, when the warm anomaly and surface low are vertically stacked. Consequently, as Velden (1992) has qualitatively demonstrated, the MSU3 T_b pattern, which is indicative of the spatial configuration of the tropopause-level thermal anomalies, should exhibit a range of phase relationships and, hence, correlations with the sea level pressure analysis depending on the stage of cyclogenesis. Over a long temporal period, which exhibits migrant baroclinic wave activity, we should therefore expect the correlations to be low.

The average 6-month spatial correlations (Table A7) bear this out. Generally poor negative correlations exist for all scales. Specifically, the average coefficient over the AL, TR, and DTR TC ≥ 0.80 groups is only -0.34. An exception to this low correlation is over area 5 (northeastern Pacific) where the AL correlation jumps to -0.75. This high correlation is possibly a reflection of the Aleutian low system.

Similarly, the temporal correlation UF and LF analyses (Figs. 17a,b) between the MSU3 T_b and sea level pressure generally indicate poor negative correlation between the MSU3 T_b and sea level pressure except in three areas: northeast of Japan, the northeastern Pacific, and the central North Atlantic. Correlations in these areas are generally better than -0.70. Again, these high correlations probably reflect the existence of the ''semipermanent'' long-wave trough and ridge systems (Holton 1979) and the associated low and high mean sea level pressures, respectively. In particular, these areas would be expected to have relatively warm (in the case of troughs) and cold (in the case of ridges) mean MSU3 T_b signatures.

The 5-day HP analysis (Fig. 17c) of MSU3 T_b and sea level pressure correlation exhibits decreased negative correlations in comparison to the lower-frequency results. As with the spatial correlation results, this general lack of temporal correlation between the MSU3 T_b and sea level pressure over most of the domain is indicative of the phasing sequence that occurs between tropopause-level anomalies and surface pressure systems during the life cycles of baroclinic waves. Only during occlusion should the warm MSU3 T_b anomalies become coincident with surface lows. Support for this hypothesis is found in the HP analyses over the areas south of the Kamchatka peninsula and the Gulf of Alaska. These locations, known as the ''graveyard'' of deep, vertically stacked occluded lows, exhibit fairly high negative correlations.

5. Summary

In this study, a 6-month climatological study was undertaken to quantitatively determine the potential usefulness of MSU3 T_b data as a nowcasting and forecasting tool. Specifically, both area-average and point temporal correlations between the NOAA polar-orbiter MSU3 T_b and various conventionally derived fields were calculated over the Northern Hemisphere midlatitudes from 1 October 1993 through 31 March 1994. In general, statistically significant correlations were found between the MSU3 T_b and various conventional fields that have been shown to be dynamically linked to the upper-level temperature field and baroclinic wave development. As expected, the strongest positive correlations existed between the MSU3 T_b and the 400–100-mb thickness field. In particular, high positive correlations (≥ 0.80) between these two fields were evident in both time and space and over all wavelengths and periods in the global data. Thus, features in the 400–100-mb thickness are readily observed by the MSU3 over the majority of the global domain and can be used with a high degree of confidence for tracking these features. Another measure of the potential usefulness of the MSU3 is to detect and track more specific thermal anomalies along the tropopause. These tropopause-level thermal anomalies have been shown by Hirschberg and Fritsch (1991a,b) and others to be important features in cyclogenesis. The ability of the MSU3 to detect and track these features is evident in the high positive temporal correlations (≥ 0.80) found between the whole spectrum of MSU3 T_b and the 200-mb temperature patterns over much of the domain.

Significantly, the 6-month results provide evidence for the LID hypothesis and the consequent thickness-spreading argument posed by Hirschberg and Fritsch (1993b). In particular, generally high positive correlations were found between the MSU3 T_bs and the 50-mb heights for wavelengths and periods greater than synoptic scale. This indicates that upper-level thermal anomalies are hydrostatically spread upward in the height field on these scales. Conversely, relatively high negative correlations were found between the MSU3 T_bs and the 500-mb heights on scales less than or equal to synoptic. This indicates that smaller-scale thermal anomalies are spread downward in the height field. Specifically, correlations ≤ -0.80 between the short-wavelength, high-frequency MSU3 T_b–500-mb heights were found over much of the midlatitudes. An exception to this was across western and central Asia where the MSU3 T_bs are possibly contaminated by surface emission or there are errors in the NCEP GDAS analyses. In addition, there were some differences between the large-scale MSU3 T_b–50-mb height spatial and temporal correlations over the Western Hemisphere. While the temporal results showed the expected high positive correlation, the spatial results displayed low correlation. The reasons for this discrepancy remain an issue for further research. Nevertheless, despite these disparities, the MSU3 indicates a

high degree of reliability for tracking synoptic-scale midlevel waves that are traditionally associated with cyclogenesis.

Important insights are also obtained from the results of the correlation between the MSU3 T_bs and the fields of midlevel vorticity and upper-level PV, which can be depicted with an analysis of the dynamic tropopause. Again, for the synoptic-scale signals, correlations of better than 0.70 were generally found over the climatological storm tracks. This linkage between the MSU3 T_bs and these important dynamical fields provides evidence that the MSU3 T_b data are potentially useful in detecting and tracking important atmospheric phenomena associated with cyclogenesis especially at off-synoptic times and over data-sparse regions. Finally, the MSU3 T_b data were found to be less useful in locating synoptic-scale sea level pressure features. This expected finding is most likely due to the phasing sequence that occurs between upper-level thermal anomalies and low-level cyclones during development.

To be complete, sources of error, not only in this study, but also in any potential operational implementation, should be considered. The most clearly identifiable problem is the contamination of the MSU3 information by surface emission. This is especially an issue over locations with relatively high topographic features such as the Tibetan plateau. This surface contamination, owing to high surface emissivity, can be compounded by coupling the MSU3 brightness temperature data with lower channels (channels 1 and 2) of the MSU via the development of statistical limb correction coefficients (Spencer and Christy 1992). Surface contamination of the MSU3 T_bs is a possible reason for the lower-than-expected spatial and temporal correlations found in the comparison of the MSU3 T_bs with conventional fields over Asia.

Other data-related error sources include instrument error in the MSU itself and any residual limb-darkening effects that are not completely corrected. There may also be errors in the data analysis procedure. In particular, phase errors certainly occur owing to the inclusion of MSU3 data over time windows (e.g., 3-h windows). The high correlation results though suggest these errors are generally small or cancel out and do not adversely impact the conclusions drawn from the spatial and temporal correlation results.

6. Conclusions

There is growing evidence that more effective use of satellite data can be made by directly utilizing the information that satellite sensors provide even if the advent of ''next generation'' satellite sounders alleviates some of the traditional low vertical resolution problems (Smith et al. 1990) associated with retrieved satellite temperature soundings. The incorporation of the measured radiance values into numerical models with sophisticated data assimilation techniques is one example of such a direct utilization. Another example is the construction of radiance analyses that illuminate specific information about the atmosphere. In particular, the results of the 6-month statistical comparison between the MSU3 T_b data and conventional fields presented in this paper suggest the usefulness of analyses of the MSU3 observations as a nowcasting and forecasting tool for tracking synoptic-scale baroclinic waves. The operational deployment of the Advanced MSU instrument with a 40-km horizontal resolution in the near future should further enhance the ability of the MSU3 in this regard.

One potential operational application of the MSU brightness temperature information is to locally collect and process the data as polar orbiters pass overhead. The resulting local MSU3 T_b analyses could then be evaluated in real time to aid in the nowcasting and forecasting of important baroclinic features in the vicinity. As a prototype for such a system, the Naval Postgraduate School currently collects and processes MSU data with commercially available equipment and produces real-time MSU3 analyses (Fig. 18) along the U.S. west coast that are available on the Internet (www.met.nps.navy.mi- l/msu.html). Similar systems could be feasibly installed at regional forecast offices for operational use and in special locations in support of field experiments. The Marshall Flight Center produces twice-daily global MSU analysis on the Internet (www.ghcc.msfc.nasa.gov/MSU/msu.html).

Another application of the MSU3 T_b data is to use them in conjunction with other data to infer further three-dimensional and dynamic information about the atmosphere. For example, information about the upper-level temperature advection pattern, which has been shown to be an important component of extratropical cyclogenesis (e.g., Hirschberg and Fritsch 1991a,b), can be obtained by combining MSU3 T_b analyses with upper-level wind information. C. S. Velden (1997, personal communication) has generated such proxy temperature advection analyses over the Northern Atlantic Ocean during the Fronts and Atlantic Storm Track Experiment by advecting MSU3 T_b fields with Geostationary Operational Environmental Satellite water vapor winds (Velden 1996; Velden et al. 1997).

Finally, this study was based on only one 6-month period during a Northern Hemisphere cold season. To extend the results reported on here, future statistical comparisons between the MSU3 T_b and conventional fields should be performed for longer periods of time that encompass the warm season. In addition, a similar study for the Southern Hemisphere would be interesting in light of the relative sparseness of conventional observations available there as compared to the Northern Hemisphere.

Acknowledgments. This work was supported by a grant from the COMET Outreach Cooperative Project and by the Naval Postgraduate School Direct Research Fund. We wish to thank Steve Drake, Kim Richardson, Charles Skupniewicz, Mrs. Penny Jones, and Chris Velden for their advice and assistance.

APPENDIX
6-month Average Area Correlations

TABLE A1. Six-month average spatial correlation coefficients between the total (AL), trend (TR) and detrend (DTR), MSU3 T_b and 400–100-mb thickness analyses for the eight areas (see Fig. 3). The coefficients are categorized for all valid times (AVT) and for times when the thickness correlation coefficient (TC) is ≥0.80 and <0.80. Standard deviations are listed for the AVT correlations (±S) and the percentage of valid map times used in the calculation of the correlation coefficients for the TC ≥ 0.80 and <0.80 groups is provided in parenthesis.

Area no.	Trend	AL	TR	DTR
1	AVT	0.86 ± 0.13	0.87 ± 0.21	0.78 ± 0.20
	TC ≥ 0.80	0.91 (78%)	0.94 (81%)	0.89 (60%)
	TC < 0.80	0.68 (22%)	0.55 (19%)	0.61 (40%)
2	AVT	0.89 ± 0.14	0.92 ± 0.13	0.73 ± 0.21
	TC ≥ 0.80	0.92 (80%)	0.96 (91%)	0.88 (50%)
	TC < 0.80	0.60 (20%)	0.58 (09%)	0.58 (50%)
3	AVT	0.90 ± 0.10	0.95 ± 0.64	0.69 ± 0.21
	TC ≥ 0.80	0.93 (88%)	0.96 (97%)	0.87 (35%)
	TC < 0.80	0.68 (12%)	0.69 (03%)	0.60 (65%)
4	AVT	0.92 ± 0.08	0.93 ± 0.08	0.82 ± 0.17
	TC ≥ 0.80	0.94 (92%)	0.95 (92%)	0.90 (69%)
	TC < 0.80	0.69 (08%)	0.70 (08%)	0.64 (31%)
5	AVT	0.88 ± 0.11	0.87 ± 0.15	0.85 ± 0.13
	TC ≥ 0.80	0.91 (85%)	0.92 (82%)	0.90 (80%)
	TC < 0.80	0.67 (15%)	0.62 (18%)	0.65 (20%)
6	AVT	0.88 ± 0.12	0.86 ± 0.18	0.88 ± 0.12
	TC ≥ 0.80	0.92 (83%)	0.93 (79%)	0.91 (88%)
	TC < 0.80	0.68 (17%)	0.59 (21%)	0.62 (12%)
7	AVT	0.86 ± 0.19	0.83 ± 0.25	0.88 ± 0.12
	TC ≥ 0.80	0.93 (80%)	0.94 (76%)	0.93 (84%)
	TC < 0.80	0.57 (20%)	0.49 (24%)	0.65 (16%)
8	AVT	0.84 ± 0.19	0.83 ± 0.24	0.83 ± 0.17
	TC ≥ 0.80	0.92 (78%)	0.93 (73%)	0.91 (74%)
	TC < 0.80	0.57 (22%)	0.56 (27%)	0.62 (26%)

TABLE A2. As in Table A1, except for MSU3 T_b and 200-mb temperature correlations. See Table A1 for the percentage of valid map times used in the calculation of the correlation coefficients for the TC ≥ 0.80 and <0.80 groups.

Area no.	Trend	AL	TR	DTR
1	AVT	0.55 ± 0.27	0.55 ± 0.37	0.59 ± 0.30
	TC ≥ 0.80	0.62	0.66	0.76
	TC < 0.80	0.28	0.06	0.34
2	AVT	0.62 ± 0.27	0.70 ± 0.32	0.57 ± 0.29
	TC ≥ 0.80	0.69	0.77	0.76
	TC < 0.80	0.16	0.01	0.39
3	AVT	0.61 ± 0.28	0.74 ± 0.26	0.50 ± 0.33
	TC ≥ 0.80	0.67	0.76	0.75
	TC < 0.80	0.18	0.37	0.38
4	AVT	0.73 ± 0.23	0.75 ± 0.27	0.65 ± 0.26
	TC ≥ 0.80	0.78	0.80	0.76
	TC < 0.80	0.23	0.23	0.41
5	AVT	0.78 ± 0.15	0.76 ± 0.24	0.76 ± 0.17
	TC ≥ 0.80	0.82	0.81	0.82
	TC < 0.80	0.55	0.52	0.55
6	AVT	0.69 ± 0.27	0.63 ± 0.36	0.74 ± 0.23
	TC ≥ 0.80	0.75	0.73	0.79
	TC < 0.80	0.41	0.26	0.35
7	AVT	0.57 ± 0.40	0.52 ± 0.47	0.68 ± 0.27
	TC ≥ 0.80	0.70	0.67	0.76
	TC < 0.80	0.07	0.06	0.27
8	AVT	0.61 ± 0.33	0.57 ± 0.40	0.62 ± 0.31
	TC ≥ 0.80	0.72	0.72	0.72
	TC < 0.80	0.22	0.15	0.35

TABLE A3. As in Table A1, except for MSU3 T_b and 500-mb height. See Table A1 for the percentage of valid map times used in the calculation of the correlation coefficients for the TC ≥ 0.80 and <0.80 groups.

Area no.	Trend	AL	TR	DTR
1	AVT	0.49 ± 0.35	0.72 ± 0.30	−0.58 ± 0.39
	TC ≥ 0.80	0.49	0.77	−0.75
	TC < 0.80	0.46	0.49	−0.34
2	AVT	0.63 ± 0.31	0.80 ± 0.25	−0.56 ± 0.37
	TC ≥ 0.80	0.62	0.81	−0.72
	TC < 0.80	0.64	0.73	−0.40
3	AVT	0.65 ± 0.25	0.75 ± 0.21	−0.52 ± 0.33
	TC ≥ 0.80	0.64	0.75	−0.70
	TC < 0.80	0.68	0.67	−0.42
4	AVT	0.23 ± 0.41	0.50 ± 0.38	−0.79 ± 0.21
	TC ≥ 0.80	0.22	0.49	−0.84
	TC < 0.80	0.30	0.56	−0.69
5	AVT	−0.75 ± 0.29	−0.64 ± 0.47	−0.84 ± 0.13
	TC ≥ 0.80	−0.77	−0.64	−0.88
	TC < 0.80	−0.61	−0.55	−0.69
6	AVT	−0.36 ± 0.58	0.27 ± 0.66	−0.78 ± 0.23
	TC ≥ 0.80	−0.41	−0.32	−0.83
	TC < 0.80	−0.17	−0.07	−0.43
7	AVT	−0.14 ± 0.61	0.03 ± 0.70	−0.70 ± 0.31
	TC ≥ 0.80	−0.28	−0.07	−0.78
	TC < 0.80	0.40	0.35	−0.31
8	AVT	−0.20 ± 0.59	−0.01 ± 0.68	−0.63 ± 0.34
	TC ≥ 0.80	−0.31	−0.11	−0.73
	TC < 0.80	0.17	0.26	−0.34

TABLE A4. As in Table A1, except for MSU3 T_b and 50-mb height. See Table A1 for the percentage of valid map times used in the calculation of the correlation coefficients for the TC ≥ 0.80 and ≤0.80 groups.

Area no.	Trend	AL	TR	DTR
1	AVT	0.79 ± 0.28	0.87 ± 0.25	0.28 ± 0.52
	TC ≥ 0.80	0.82	0.92	0.19
	TC < 0.80	0.70	0.65	0.40
2	AVT	0.83 ± 0.22	0.91 ± 0.19	0.23 ± 0.52
	TC ≥ 0.80	0.84	0.92	0.11
	TC < 0.80	0.76	0.81	0.35
3	AVT	0.86 ± 0.15	0.90 ± 0.13	0.29 ± 0.42
	TC ≥ 0.80	0.86	0.91	0.29
	TC < 0.80	0.82	0.77	0.29
4	AVT	0.67 ± 0.30	0.78 ± 0.24	0.33 ± 0.40
	TC ≥ 0.80	0.68	0.78	0.35
	TC < 0.80	0.52	0.73	0.27
5	AVT	−0.02 ± 0.45	0.01 ± 0.57	−0.07 ± 0.44
	TC ≥ 0.80	0.00	0.07	−0.05
	TC < 0.80	−0.16	−0.24	−0.12
6	AVT	0.08 ± 0.53	0.08 ± 0.62	0.07 ± 0.47
	TC ≥ 0.80	0.04	0.04	0.05
	TC < 0.80	0.28	0.25	0.28
7	AVT	0.20 ± 0.61	0.24 ± 0.69	0.31 ± 0.50
	TC ≥ 0.80	0.09	0.15	0.30
	TC < 0.80	0.60	0.49	0.36
8	AVT	0.13 ± 0.61	0.22 ± 0.68	0.23 ± 0.51
	TC ≥ 0.80	0.04	0.13	0.22
	TC < 0.80	0.44	0.45	0.24

TABLE A5. As in Table A1, except for MSU3 T_b and 500-mb vorticity. See Table A1 for the percentage of valid map times used in the calculation of the correlation coefficients for the TC $>$ 0.80 and $\geq$ 0.80 groups.

Area no.	Trend	AL	TR	DTR
1	AVT	−0.09 ± 0.31	−0.38 ± 0.33	0.48 ± 0.22
	TC ≥ 0.80	−0.10	−0.41	0.56
	TC < 0.80	−0.42	−0.23	0.34
2	AVT	−0.16 ± 0.28	−0.41 ± 0.32	0.47 ± 0.21
	TC ≥ 0.80	−0.14	−0.40	0.53
	TC < 0.80	−0.30	−0.55	0.00
3	AVT	−0.23 ± 0.27	−0.42 ± 0.30	0.39 ± 0.23
	TC ≥ 0.80	−0.22	−0.43	0.45
	TC < 0.80	−0.27	−0.34	0.36
4	AVT	0.06 ± 0.29	−0.28 ± 0.35	0.56 ± 0.16
	TC ≥ 0.80	0.06	−0.27	0.61
	TC < 0.80	−0.02	−0.31	0.43
5	AVT	0.65 ± 0.16	0.59 ± 0.32	0.59 ± 0.16
	TC ≥ 0.80	0.68	0.45	0.63
	TC < 0.80	0.50	0.47	0.45
6	AVT	0.44 ± 0.38	0.34 ± 0.51	0.54 ± 0.21
	TC ≥ 0.80	0.48	0.39	0.57
	TC < 0.80	0.26	0.17	0.31
7	AVT	0.33 ± 0.47	0.14 ± 0.60	0.55 ± 0.19
	TC ≥ 0.80	0.44	0.23	0.58
	TC < 0.80	−0.10	−0.15	0.39
8	AVT	0.34 ± 0.44	0.14 ± 0.58	0.51 ± 0.22
	TC ≥ 0.80	0.43	0.24	0.58
	TC < 0.80	0.03	−0.13	0.31

TABLE A6. As in Table A1, except for MSU3 T_b and dynamic tropopause. See Table A1 for the percentage of valid map times used in the calculation of the correlation coefficients for the TC $\geq$ 0.80 and $<$0.80 groups.

Area no.	Trend	AL	TR	DTR
1	AVT	−0.01 ± 0.32	−0.29 ± 0.36	0.47 ± 0.24
	TC ≥ 0.80	0.00	−0.30	0.57
	TC < 0.80	−0.05	−0.26	0.32
2	AVT	−0.11 ± 0.31	−0.37 ± 0.36	0.43 ± 0.25
	TC ≥ 0.80	−0.08	−0.35	0.53
	TC < 0.80	−0.32	−0.55	0.33
3	AVT	−0.22 ± 0.32	−0.45 ± 0.31	0.38 ± 0.28
	TC ≥ 0.80	−0.21	−0.44	0.49
	TC < 0.80	−0.32	−0.47	0.32
4	AVT	0.04 ± 0.31	−0.33 ± 0.36	0.55 ± 0.20
	TC ≥ 0.80	0.05	−0.33	0.60
	TC < 0.80	0.15	−0.43	0.42
5	AVT	0.66 ± 0.17	0.60 ± 0.33	0.60 ± 0.18
	TC ≥ 0.80	0.70	0.63	0.65
	TC < 0.80	0.47	0.45	0.42
6	AVT	0.43 ± 0.39	0.30 ± 0.51	0.50 ± 0.24
	TC ≥ 0.80	0.47	0.36	0.53
	TC < 0.80	0.23	0.11	0.26
7	AVT	0.29 ± 0.45	0.14 ± 0.54	0.46 ± 0.25
	TC ≥ 0.80	0.40	0.25	0.50
	TC < 0.80	−0.12	−0.17	0.23
8	AVT	0.34 ± 0.45	0.15 ± 0.58	0.48 ± 0.29
	TC ≥ 0.80	0.44	0.27	0.56
	TC < 0.80	−0.02	−0.16	0.25

TABLE A7. As in Table A1, except for MSU3 T_b channel 3 and sea level pressure. See Table A1 for the percentage of valid map times used in the calculation of the correlation coefficients for the TC $\geq$ 0.80 and $<$0.80 groups.

Area no.	Trend	AL	TR	DTR
1	AVT	−0.29 ± 0.52	−0.18 ± 0.64	−0.21 ± 0.43
	TC ≥ 0.80	−0.30	−0.19	−0.30
	TC < 0.80	−0.24	−0.16	−0.06
2	AVT	−0.28 ± 0.36	−0.26 ± 0.49	−0.08 ± 0.42
	TC ≥ 0.80	−0.28	−0.27	−0.20
	TC < 0.80	−0.26	−0.13	0.03
3	AVT	−0.09 ± 0.43	−0.10 ± 0.56	−0.11 ± 0.39
	TC ≥ 0.80	−0.10	−0.11	−0.17
	TC < 0.80	−0.09	0.21	−0.08
4	AVT	−0.42 ± 0.38	−0.48 ± 0.42	−0.32 ± 0.36
	TC ≥ 0.80	−0.41	−0.49	−0.36
	TC < 0.80	−0.49	−0.27	−0.24
5	AVT	−0.74 ± 0.23	−0.65 ± 0.36	−0.70 ± 0.22
	TC ≥ 0.80	−0.75	−0.66	−0.73
	TC < 0.80	−0.65	−0.60	−0.60
6	AVT	−0.25 ± 0.38	−0.20 ± 0.47	−0.31 ± 0.35
	TC ≥ 0.80	−0.26	−0.22	−0.32
	TC < 0.80	−0.21	−0.13	−0.22
7	AVT	−0.23 ± 0.44	−0.12 ± 0.57	−0.27 ± 0.43
	TC ≥ 0.80	−0.32	−0.18	−0.29
	TC < 0.80	0.10	0.06	−0.14
8	AVT	−0.34 ± 0.48	−0.19 ± 0.61	−0.39 ± 0.44
	TC ≥ 0.80	−0.43	−0.29	−0.47
	TC < 0.80	−0.01	0.07	−0.16

REFERENCES

Barnes, S. L., 1973: Mesoscale objective analysis using weighted time-series observations. NOAA Tech. Memo. ERL NSSL-62, 60 pp. [NTIS COM-73-10781.]

Bell, G. D., and L. F. Bosart, 1993: A case study diagnosis of the formation of an upper-level cutoff cyclonic circulation over the eastern United States. *Mon. Wea. Rev.*, **121,** 1635–1655.

Claud, C., K. B. Katsaros, N. M. Mognard, and N. A. Scott, 1995: Synergetic satellite study of a rapidly deepening cyclone over the Norwegian Sea: 13–16 February 1989. *Global Atmos. Ocean Syst.*, **3,** 1–34.

Cressman, G. P., 1959: An operational objective analysis system. *Mon. Wea. Rev.*, **87,** 367–374.

Dixon, W. J., and F. J. Massey Jr., 1969: *Introduction to Statistical Analysis.* McGraw-Hill, 638 pp.

Errico, R. M., 1985: Spectra computed from a limited area grid. *Mon. Wea. Rev.*, **113,** 1554–1562.

Eyre, J. R., and A. C. Lorenc, 1989: Direct use of satellite sounding radiances in numerical weather prediction. *Meteor. Mag.*, **118,** 13–16.

Flobert, J.-F., E. Andersson, A. Chedin, A. Hollingsworth, G. Kelly, J. Pailleux, and N. A. Scott, 1991: Global data assimilation and forecast experiments using the improved initialization inversion method for satellite soundings. *Mon. Wea. Rev.*, **119,** 1881–1914.

Hirschberg, P. A., and J. M. Fritsch, 1991a: Tropopause undulations and the development of extratropical cyclones. Part I: Overview and observations from a cyclone event. *Mon. Wea. Rev.*, **119,** 496–517.

——, and ——, 1991b: Tropopause undulations and the development of extratropical cyclones. Part II: Diagnostic analysis and conceptual model. *Mon. Wea. Rev.*, **119,** 518–550.

——, and ——, 1993a: A study of the development of extratropical cyclones with an analytic model. Part I: The effects of stratospheric structure. *J. Atmos. Sci.*, **50,** 311–327.

——, and ——, 1993b: On understanding height tendency. *Mon. Wea. Rev.*, **121,** 2646–2661.

——, and ——, 1994: A study of the development of extratropical cyclones with an analytic model. Part II: Sensitivity to tropospheric structure and analysis of the height tendency dynamics. *Mon. Wea. Rev.*, **122,** 2312–2330.

——, and J. D. Doyle, 1995: An examination of pressure tendency mechanisms in an idealized simulation of extratropical cyclogenesis. *Tellus*, **47A,** 747–758.

Holton, J. R., 1979: *An Introduction to Dynamic Meteorology*. Academic Press, 391 pp.

Hoskins, B. J., and P. Berrisford, 1988: A potential vorticity perspective of the storm of 15–16 October 1987. *Weather*, **43,** 122–129.

——, M. E. McIntyre, and A. W. Robertson, 1985: On the use and significance of isentropic potential vorticity maps. *Quart. J. Roy. Meteor. Soc.*, **111,** 877–946.

Jusem, J. C., and R. Atlas, 1991: Diagnostic evaluation of numerical model simulations using the tendency equation. *Mon. Wea. Rev.*, **119,** 2936–2955.

Kanamitsu, M., 1989: Description of the NMC Global Data Assimilation and Forecast System. *Wea. Forecasting*, **4,** 335–342.

Lupo, A. R., P. J. Smith, and P. Zwack, 1992: A diagnosis of the explosive development of two extratropical cyclones. *Mon. Wea. Rev.*, **120,** 1490–1523.

Martin, J. E., J. D. Locatelli, and P. V. Hobbs, 1993: Organization and structure of clouds and precipitation on the mid-Atlantic coast of the United States. Part VI: The synoptic evolution of a deep tropospheric frontal circulation and attendant cyclogenesis. *Mon. Wea. Rev.*, **121,** 1299–1316.

Nuss, W. A., and D. W. Titley, 1994: Use of multiquadric interpolation for meteorological objective analysis. *Mon. Wea. Rev.*, **122,** 1611–1631.

Petterssen, S., 1956: *Weather Analysis and Forecasting*. 2d ed. McGraw-Hill, 428 pp.

Rao, P. K., S. J. Holmes, R. K. Anderson, J. S. Winston, and P. E. Lehr, 1990: *Weather Satellites: Systems, Data, and Environmental Application*. Amer. Meteor. Soc., 503 pp.

Shapiro, M. A., A. J. Krueger, and P. J. Kennedy, 1982: Nowcasting the position and intensity of jet streams using a satellite-borne total ozone mapping spectrometer. *Nowcasting*, K. A. Browning, Ed., Academic Press, 137–145.

Smith, W. L., and Coauthors, 1990: GHIS—The Goes High-Resolution Interferometer Sounder. *J. Appl. Meteor.*, **29,** 1189–1204.

Spencer, R. W., and J. R. Christy, 1992: Precision and radiosonde validation of satellite gridpoint temperature anomalies. Part I: MSU channel 2. *J. Climate*, **5,** 847–857.

——, ——, and N. C. Grody, 1990: Global atmospheric temperature monitoring with satellite microwave measurements: Method and results, 1979–84. *J. Climate*, **3,** 1111–1128.

——, W. M. Lapenta, and F. R. Robertson, 1995: Vorticity and vertical motions diagnosed from satellite deep layer temperatures. *Mon. Wea. Rev.*, **123,** 1800–1810.

Uccellini, L. W., D. Keyser, K. F. Brill, and C. H. Wash, 1985: The Presidents' Day cyclone of 1–19 February 1979: Influence of upstream trough amplification and associated tropopause folding on rapid cyclogenesis. *Mon. Wea. Rev.*, **113,** 962–988.

Velden, C. S., 1992: Satellite-based microwave observations of tropopause-level thermal anomalies: Qualitative applications in extratropical cyclones events. *Wea. Forecasting*, **7,** 669–682.

——, 1996: Winds derived from geostationary satellite moisture channel observations: Applications and impact on numerical weather prediction. *Meteor. Atmos. Phys.* **60,** 37–46.

——, C. M. Hayden, S. J. Nieman, W. P. Menzel, S. Wanzong, and J. S. Goerss, 1997: Upper-tropospheric winds derived from geostationary satellite water vapor observations. *Bull. Amer. Meteor. Soc.*, **78,** 173–195.

Yates, W., and A. Bateman, 1989: *Digital Signal Processing Design*. Computer Science Press, 345 pp.